Theoretical Techniques for the Study of Bonding, Vibrations, and Structures of Water-Ion Clusters

by

Elva V Henderson

B.S., North Dakota State University, 2016

Submitted to the Graduate Faculty of

the Dietrich School of Arts and Sciences in partial fulfillment

of the requirements for the degree of

Doctor of Philosophy

University of Pittsburgh

2022

UNIVERSITY OF PITTSBURGH

DIETRICH SCHOOL OF ARTS AND SCIENCES

This dissertation was presented

by

Elva V Henderson

It was defended on

July 21st 2021

and approved by

Kenneth Jordan, Department of Chemistry

Sean Garret-Roe, Department of Chemistry

Geoffrey Hutchison, Department of Chemistry

John Keith, Department of Chemical Engineering

Theoretical Techniques for the Study of Bonding, Vibrations, and Structures of Water-Ion Clusters

Elva V Henderson, PhD

University of Pittsburgh, 2022

For decades, experimentalists and theoreticians have used gas-phase water-ion clusters to probe solute-solvent interactions at a molecular level. Vibrational spectroscopy on these clusters has yielded a wealth of information of the structure and dynamics of these small systems. This information can then be used to gain insight into the solvation interactions in a bulk system. However, despite their small size, these clusters are surprisingly complex, and much is still to be learned about these systems.

This work explores two contrasting approaches to the computational study of water-ion clusters. The first approach is the use of experimental references to build upon and expand theoretical techniques. The property of interest is vibrational progressions in the OH stretching regions of water-anion clusters of the form $X^- \cdot (H_2O)$ (where X^- is a polyatomic anion). This progression arises from a coupling of the high-frequency OH stretching modes with low-frequency intermolecular rock modes. Although previous theoretical models have been able to qualitatively reproduce these progressions, obtaining quantitative agreement with experiment has proven more difficult. To tackle this problem, a one-dimensional adiabatic model was developed to directly model the effect of OH stretch excitation on the rocking mode. This model was further expanded into a two-dimensional model to reproduce these progressions with even greater accuracy.

The second approach is the use of computational techniques to aid in the interpretation and understanding of new experimental results on protonated water clusters. Experiments were performed by the Johnson group to observe the migration of a hydrogen atom over time in the $D_3O^+ \cdot (HDO)(D_2O)_{19}$ cluster. These experiments showed that when the HOD monomer had a free OD stretch, the cluster could undergo an interconversion to yield a free OH stretch. A mix of computational techniques was used to confidently determine the pathway of this interconversion, in which the cluster goes through an intermediate state

containing a four-membered ring.

Table of Contents

List of Tables

List of Figures

Preface

I remember my first day in the Pitt grad program. I was 1,000 miles away from anyone I knew and living in a totally unfamiliar city. I was nervous and outside of my comfort zone, but I was excited for this new adventure. There were ups and downs, there were exciting new opportunities, and there was a significant amount of self-discovery. Looking back on it, I can't help but feeling grateful for all the experiences and how they helped me grow into the person I am today. And as this adventure is drawing to a close, I want to thank all of the people who helped me get here.

Thank you to my family and all the support they provided from the beginning, even as I moved halfway across the country away from them. Knowing that they had my back made it possible for me to take this big leap into the unknown. Thank you to the friends I made at Pitt, who quickly made this place feel like home. Thank you to Kevin, who managed to tolerate living with me for two whole years.

I want to thank all the people who I was lucky enough to work with during my stay at Pitt. Thank you to all the Jordan group members, past and present, for all of your assistance, feedback, and help you enthusiastically provided. Thank you to Tae Hoon, for sticking with me on the extremely long Water 21 project. Thank you to the collaborators I worked with for letting me be a part of all the incredible science you do. Special thanks to the members of the Johnson group from Yale, whose work on water clusters provided the experimental basis for my own research. Most of all, thank you to Ken, for all of guidance and patience over my journey, and for introducing me to fascinating and wonderful types of chemistry that I had never given much thought to prior to working with you.

Finally, I want to thank Elli, who gave me the final push to get this done, and made me excited for all the new adventures ahead.

1.0 Introduction

1.1 Vibrational Theory

1.1.1 The Harmonic Oscillator Approximation

A simple harmonic oscillator in classical physics can be visualized as two masses attached by a spring. The spring exerts a force on the masses as they are displaced from their equilibrium distance r_0. For a harmonic oscillator, this force is proportional to the displacement from equilibrium:

$$F = -k(r - r_0) = -kx$$

where k is the force constant, and can be thought of as the "stiffness" of the spring. The motion of the spring over time starting from equilibrium can be described as follows:

$$x(t) = A\cos(\omega t)$$

where A is the amplitude of the motion and ω is the angular frequency of the oscillation described as follows:

$$\omega = \sqrt{\frac{k}{\mu}}$$

and μ is the reduced mass of the system. In the absence of other forces, the masses will move back and forth in a perfectly harmonic motion, hence the name "harmonic oscillator". The true power of these equations is that they can be used to describe many classical systems with harmonic motion, even those that scarcely resemble the simple spring system.

1.1.2 The Quantum Harmonic Oscillator

The simplicity and broad applicability of the harmonic oscillator led to it being one of the first systems studied in the development of quantum mechanics. Both Bohr[1] and

Heisenberg[2] examined the system in some of the earliest quantum mechanics papers. The potential energy function $V(x)$ is identical to the classical system:

$$V(x) = \frac{1}{2}kx^2 = \frac{1}{2}m\omega^2x^2$$

Thus, the Hamiltonian of the one-dimensional quantum harmonic oscillator is:

$$\hat{H} = -\frac{\hbar^2}{2m}\frac{d^2}{dx^2} + \frac{1}{2}kx^2$$

The quantum harmonic oscillator has the advantage of being one of the few quantum-mechanical systems that is possible to solve exactly. The wavefunction consists of a Gaussian function multiplied by a Hermite polynomial. The energy levels are as follows:

$$E_n = \hbar\omega(n + 1/2),\ n = 0, 1, 2...$$

There are two interesting features of these energy levels. First, the energy levels are evenly spaced. Second, the ground state energy is greater than zero, meaning there is always vibrational energy in the molecule, even at 0 K.

A widespread application of the quantum harmonic oscillator is in describing molecular vibrations. Using force constants derived from electronic structure calculations, it is possible to obtain energy levels which are within 5% of experimental values for many chemically important vibrations. In particular, calculated values for stretching modes, such as OH stretch or CH stretch, often reproduce qualitative trends in the experiment. Applications for these calculations include aiding molecule identification, determining thermodynamic values, and investigating molecular struture, among many others.

1.1.3 Normal Mode Approximation

While calculating the vibrational levels of a diatomic molecule is fairly trivial, a more involved approach is required for polyatomic molecules. To start, it is no longer possible to reduce intramolecular motion to a single coordinate. There are a total of $3N$ atomic coordinates in any molecule, where N is the number of atoms, corresponding to the motion of each individual atom in the x, y, or z direction. However, this is not very useful for molecular vibrations, since they tend to involve the motion of multiple atoms simultaneously. Thus, we seek to find a linearly independent coordinate system where each coordinate corresponds to a molecular motion. 3 coordinates will correspond to molecular translations, 3 coordinates correspond to molecular rotations (2 in a linear molecule), and the remaining $3N - 6$ coordinates correspond to intramolecular motion ($3N - 5$ in a linear molecule).

One set of coordinates that fit these requirements is called the normal modes of a molecule [3–5]. To find the normal modes, the Hessian matrix H must be calculated. This is a matrix of the second derivatives of electronic energy with respect to atomic coordinates:

$$H_{ij} = \frac{\partial^2 E}{\partial x_i \partial x_j}$$

This is then converted into the mass-weighted Hessian matrix H^m:

$$H^m_{ij} = \frac{H_{ij}}{\sqrt{m_i * m_j}}$$

where x_i is the x, y, or z Cartesian coordinate of a single atom, and m_i is the mass of the atom associated with this coordinate. Diagonalization of this matrix will give a set of normal modes and their force constants. These force constants create a set of $3N$ harmonic potentials (including 3 translational modes and 3 rotational modes), from which harmonic frequencies can be readily calculated.

Harmonic normal mode frequencies provide a reasonable approximation for many high frequency vibrations. For example, OH stretch harmonic frequencies are generally within 5% of experimental values. The level of accuracy and the ease of computation has led to a wide use of harmonic normal modes for a wide variety of systems. However, they are often not adequate for highly anharmonic vibrations or when a high degree of accuracy is required. Therefore, there is a lot of interest in alternate approaches.

There are various methods for adding anharmonic corrections to harmonic normal mode frequencies. These include vibrational perturbation theory, vibrational SCF, and vibrational CI. These methods all require expanding the harmonic normal mode potentials with higher order terms. Generally, these are obtained using a Taylor series expansion with respect to the normal modes to obtain cubic, quartic, and higher terms, including terms involving multiple modes. These potentials can then be used to solve for anharmonic frequencies using the methods previously listed. While all of these methods operate differently and have different computational requirements, they are all limited in accuracy by the accuracy of the Taylor series expansion of the potential. Even vibrational CI, which can theoretically give exact anharmonic frequencies, can run into issues when approximations are made to the form of the potential energy surface. Issues most commonly arise from an inability to calculate sufficiently high order terms of the potential or computational limits in the accuracy of higher order derivatives. Therefore, for many systems, it is preferable to use alternate methods for calculating anharmonic frequencies that are not based on normal mode coordinates.

1.1.4 Relaxed Scan Coordinates

The harmonic normal mode approximation generally works well for high frequency vibrations with relatively low anharmonicity. However, it has some important limitations. In particular, the approximation does poorly for large amplitude motions. This is because the normal modes are calculated using only the second energy derivatives at the equilibrium geometry, and thus cannot accurately predict the potential energy surface for large displacements from this geometry.

In a relaxed scan, a potential energy surface is constructed by calculating the energy at a series of points along the coordinates of interest. At each point, the coordinates of interest are fixed while all other degrees of freedom are optimized. Compared to normal modes, this gives a more realistic view of large amplitude motions, as the relaxation of the molecule means that coupling with the other motions is implicitly accounted for. Relaxed scans can provide far more accurate frequencies for large amplitude vibrations than other techniques. However, to achieve this accuracy, it is important to accurately calculate the kinetic energy of the vibration. In a relaxed scan, the displacement of atoms may vary non-linearly along the scan coordinates. This means a more involved approach for treating reduced mass is required, which will be addressed in the next section.

1.1.5 The Wilson G-Matrix

In the normal mode approximation, atomic displacements x_i vary linearly with respect to a normal coordinate q. In other words

$$\frac{\partial}{\partial q} x_i = c$$

for all values of q, where c is a constant. This allows a constant value to be used for reduced mass. However, this is not necessarily true in other coordinate systems, particularly in a relaxed scan. In addition, if coordinates are not linearly independent, then we have to consider kinetic coupling between coordinates. Thus, a general formulation of reduced mass which can be used with any arbitrary coordinate system is desirable.

The Wilson G-Matrix procedure is a procedure used to calculate the kinetic energy of intramolecular motions for an arbitrary coordinate system[6]. Podolski introduced a form of the kinetic energy operator in generalized internal coordinates[7]:

$$T_q = \frac{-\hbar^2}{2} \sum_{r=1}^{M} \sum_{s=1}^{M} \left[g^{1/4} \frac{\partial}{\partial q_r} \left[g^{-1/2} \cdot G^{rs} \frac{\partial}{\partial q_s} \left[g^{1/4} \right] \right] \right]$$

where q_r is a generic internal coordinate, M is the total number of internal coordinates of interest, G^{rs} is a term in the Wilson G-Matrix, and g is its determinant. The terms G^{rs} are calculated as follows:

$$G^{rs} = \sum_{i=1}^{3N} m_i \left[\frac{\partial q_r}{\partial x_i} \right] \left[\frac{\partial q_s}{\partial x_i} \right]$$

where x_i is an atomic Cartesian coordinate, m_i is the mass of atom i, and N is the total number of atoms. The diagonal elements of this matrix correspond to the inverse reduced masses:

$$G^{rr} = \frac{1}{\mu_r}$$

and the off-diagonal elements are kinetic coupling terms. Often, it is more convenient to calculate the elements of the inverse G-Matrix:

$$G_{rs} = \sum_{i=1}^{3N} \frac{1}{m_i} \left[\frac{\partial x_i}{\partial q_r}\right] \left[\frac{\partial x_i}{\partial q_s}\right]$$

Inverting this matrix will yield the standard G-Matrix.

It's important to note that the values G^{rs} (and therefore g) are not necessarily constant with respect to the internal coordinates. If this is the case, then the reduced masses of the modes are effectively functions which vary with respect to the coordinates q. In cases where the off-diagonal elements of the G-Matrix are zero, then the reduced mass for mode r will only depend on q_r. However, if the off-diagonal elements are nonzero, this creates kinetic coupling between the modes, and the reduced mass is a function of all coordinates.

One technique which can simplify the calculation of the Wilson G-Matrix is to remove translational and rotational contributions by enforcing the Eckart frame[8, 9]. To remove translational contribution, the center of mass is kept fixed along q_r:

$$\sum_{i=1}^{3N} \frac{m_i x_i}{m_{tot}} = 0$$

To remove rotational motion, a reference geometry is used (usually the equilibrium geometry of the molecule for convenience) with coordinates R. Motions along q_r are compared to the reference coordinates with a displacement vector $\boldsymbol{d}$ for each atom A:

$$\boldsymbol{d}_A = x_A - R_A$$

The displaced geometry is then rotated such that

$$\sum_{A=1}^{N} m_A \left(R_A \cdot \boldsymbol{d}_A\right) = 0$$

By enforcing the Eckart frame, we ensure that there is no kinetic coupling between external and internal motion, allowing us to consider only the $3N - 6$ internal coordinates. The G-Matrix can be further simplified by only looking at a subset of internal modes. This is the approach generally taken when doing relaxed scans along a small number of coordinates.

1.2 Discrete Variable Representation

Most methods of calculating quantum mechanical energy levels assume a specific form of the potential energy operator, usually a form that can be solved exactly or one where approximate solutions have been discovered. However, in many circumstances, it is useful to have a technique which can be used to solve for an arbitrary potential energy surface. This motivated the development of discrete variable representation (DVR) methods[10]. DVR methods use a grid based basis set where the potential energy matrix $V_{ij} = \langle i| \hat{V} |j\rangle$ is diagonal. Numerous implementations of DVR with different basis sets have been developed, such as sine functions, harmonic oscillator basis functions, or delta functions. Different types of DVR have different advantages which make them suitable for different types of problems.

One type of DVR which has been previously used for highly anharmonic vibrational systems is Fourier Grid Hamiltonian Discrete Variable Representation (FGH-DVR)[11, 12]. FGH-DVR uses a basis of Dirac Delta functions:

$$\delta(x' - x) = \begin{cases} 1, & x = x' \\ 0, & x \neq x' \end{cases}$$

To obtain the kinetic energy terms, these functions are transformed into momentum space:

$$\delta(x' - x) = \frac{1}{2\pi} \int_{k=-\infty}^{\infty} e^{-ik(x'-x)} dk$$

Next, both x and k are discretized on uniform grids. For a grid from 0 to L with N grid points, the grid spacing along x is $\Delta x = L/N$. The momentum grid ranges from $k = -n\Delta k$ to $k = n\Delta k$ where $\Delta k = 2\pi/L$ and $n = (N-1)/2$. Note that this setup is for an odd number of grid points, and the final terms are slightly different for an even number of grid points. From this point, it is possible to derive the derivative terms in the kinetic energy matrix. The following form is used for the second derivative terms[11]:

$$\left[\frac{\partial^2}{\partial^2 x}\right]_{j,t} = \begin{cases} -\left(\frac{2\pi}{L}\right)^2 \frac{n(n+1)}{3}, & j = t \\ -\left(\frac{2\pi}{L}\right)^2 \frac{(-1)^{(t-j)}(n+1)cos[A]+(n+1)cos[2(n+1)A]-sin[2(n+1)A]cot[A]}{2N sin^2[A]}, & j \neq t \end{cases}$$

where $A = \frac{(t-j)\pi}{N}$. With these terms, a Hamiltonian matrix can be constructed, which yields the energy levels of the system upon diagonalization. The advantages of FGH-DVR are that it gives accurate results for a variety of shapes of potentials, the elements of the Hamiltonian matrix are relatively easy to compute, and it can be expanded into multidimensional grids without substantially altering the computation.

1.3 Water Clusters and Water-Ion Clusters

Water is one of the most common compounds on earth, and is critically important in biology and chemistry. It's small size and large dipole moment make it a very effective polar solvent, leading water to often be referred to as the "universal solvent." Despite the simplicity of the molecule, water systems can be extremely complex. This is owing to the bent geometry and high dipole moment, which causes water to form large hydrogen bonded networks with other water molecules. This also applies to water-solute systems, which often involve multiple solvation shells. It is difficult to study these water-solute interactions in detail in a bulk system due to the sheer number of molecules. Therefore, it is useful to study smaller systems with relatively few water and solute molecules to gain insight into the bulk system.

To produce water clusters experimentally, gas phase clusters of a variety of sizes are produced through techniques such as electrospray[13] or ionizing a gaseous mixture with an electron beam[14]. Some experimental setups may introduce a gas "tag", such as Ar or H_2, which binds weakly to the cluster through dispersion forces. Then, mass spectrometry is used to isolate the cluster of the desired size.

One common way to study water clusters is through infrared spectroscopy. If a cluster absorbs a photon of high enough energy, the temperature of the cluster will increase to the point that the cluster will fragment. A second mass spectrometer can then be used to measure the proportion of clusters that disassociated, giving a relative absorbance for that transition. The obvious limitation of this technique is that if the energy of the photon is not sufficient to dissociate the cluster, then it is impossible to determine if absorption has occurred or not. This is why tagging atoms or molecules are often included: the tag is bound much more weakly than the other species in the cluster, meaning even absorption of low frequency photons can add enough energy to the cluster to cause dissociation of the tag[14, 15]. For studies focused on high frequency vibrations, such as OH stretching modes, the energy of the photon may be high enough that a tag is unnecessary.

1.3.1 Water-Anion Clusters

Another popular area of research is using water-ion clusters to study the solvation of anions in an aqueous solution. One of the first water-anion clusters to be studied experimentally was $I^- \cdot (H_2O)$ to determine whether the cluster contains one or two hydrogen bonds[16]. Over time,experimental methods improved and more clusters were studied, including those with polyatomic anions and more H_2O monomers. In 2003, Robertson et al. discovered that, instead of the expected one or two peaks, the clusters ${CH_3NO_2}^- \cdot (H_2O)$ and ${CH_3CO_2}^- \cdot (H_2O)$ contained five peaks in the OH stretching region of their infrared spectra[14]. Similar features were later found in the spectra of ${NO_3}^- \cdot (H_2O)$[13] and ${HCO_2}^- \cdot (H_2O)$[17, 18]. Robertson et al. proposed that these OH stretch progressions could be partially explained using an adiabatic rock potential along the intermolecular rock coordinate, θ:

$$V(\theta) = V_{BO}(\theta) + (N_1 + \frac{1}{2})\hbar\omega_1(\theta) + (N_2 + \frac{1}{2})\hbar\omega_2(\theta)$$

where V_{BO} is the ab initio energy in the Born-Oppenheimer approximation, N_1 and N_2 are the number of quanta in each OH stretch vibration, and ω_1 and ω_2 are their associated frequencies[14]. These potentials showed that the minimum energy of the adiabatic potentials were at $\theta = 0$ when $N_1 = N_2 = 0$, but shifted upon excitation of the OH stretch. Robertson et al. predicted that the excitation of the OH stretch would cause a structural change in the cluster, creating a "Franck-Condon" like overlap in the rock mode from the two potentials, resulting in the observed progression. However, the authors were unable to show this conclusively, and encouraged other researchers to study it with a more in depth theoretical analysis.

This progression would next be studied by Myshakin et al. later that year[19]. Adiabatic rock potentials for ${CH_3NO_2}^- \cdot (H_2O)$ and ${CH_3CO_2}^- \cdot (H_2O)$ were again created, but instead of explicitly calculating the potentials at different points along θ, a model Hamiltonian was used[19]:

$$\hat{H} = \frac{\hat{p}_A^2}{2} + \frac{\hat{p}_S^2}{2} + \frac{\hat{p}_R^2}{2} + \frac{\omega_A^2}{2}Q_A^2 + \frac{\omega_S^2}{2}Q_S^2 + \frac{\omega_R^2}{2}Q_R^2 + \lambda Q_A Q_S Q_R$$

where Q_A, Q_S, and Q_R are the normal mode coordinates for the asymmetric OH stretch, the symmetric OH stretch, and the intermolecular rock mode, respectively. By transforming the symmetric and asymmetric OH stretch into a local modes, Myshakin et al. were able to derive a set of rock potential energy curves for the number of quanta in each OH stretch:

$$V_R(0,0) = \frac{\omega_R^2}{2}Q_R^2 + \hbar\omega_L$$

$$V_R(1,0) = \frac{\omega_R^2}{2}Q_R^2 + \frac{\hbar\lambda}{2\omega_L}Q_R + 2\hbar\omega_L$$

$$V_R(0,1) = \frac{\omega_R^2}{2}Q_R^2 - \frac{\hbar\lambda}{2\omega_L}Q_R + 2\hbar\omega_L$$

where ω_L is the local mode OH stretch frequency:

$$\omega_L = \sqrt{\frac{\omega_S^2 + \omega_A^2}{2}}$$

This gives a set of displaced harmonic potential energy curves. The energy levels for the transition from the ground state of the $V_R(0,0)$ potential to various levels in the $V_R(1,0)$ and $V_R(0,1)$ potentials is:

$$E(n_R) = \hbar\omega_L - \frac{\hbar^2\lambda^2}{8\omega_L^2\omega_R^2} + \hbar\omega_R n_R$$

Notably, the energies of the transitions are evenly spaced and equal to the harmonic rock frequency.

The model of Myshakin et al. does a good job of qualitatively reproducing the observed spectra in these clusters, and its simplicity makes it easy to apply to a variety of systems. However, it has some notable limitations. It neglects any anharmonic coupling aside from a single rock-stretch term, which may not be an accurate assumption for many systems. It is also unable to reproduce any spectra where the peaks are not evenly spaced. Thus, more rigorous treatments have been explored to achieve better quantitative accuracy.

In 2015, Hamm and Stock developed an extension of these adiabatic models for the cluster $HCO_2{}^- \cdot (H_2O)$[20]. Unlike the prior models, which modeled the coupling between three vibrational modes, Hamm and Stock modeled the coupling between six modes: the two water OH stretches, the water bend, the intermolecular separation mode, and two intermolecular rock modes (essentially the water rock and the $HCO_2{}^-$ rock). An adiabatic separation was performed between the high frequency intramolecular modes and the low frequency intermolecular modes. A three-dimensional grid along the intermolecular modes was formed, with the Born-Oppenheimer energy calculated at each grid point. To determine the energy of the high-frequency modes, a power series expansion along the high frequency coordinates was performed. To obtain the coefficients of the expansion, additional energy calculations were performed. The energy levels were calculated by diagonalizing a Hamiltonian matrix using harmonic oscillator basis sets along the three modes. This procedure needed to be performed at every point in the grid of low frequency modes. Spectra were calculated using a few different techniques, including DVR and time-dependent vibrational dynamics[20].

The model of Hamm and Stock provided excellent agreement with experimental results, and provided valuable insight into the nature of vibrational coupling in water-anion clusters. The model showed conclusively that vibrational progressions in $HCO_2{}^- \cdot (H_2O)$ were predominantly due to the coupling of the OH stretch and water rock modes, as assumed by prior models. However, it also showed that there was significant coupling between the OH stretch and the anion rock modes, which had not been explored previously.

While the model of Hamm and Stock is very accurate, the computational cost of that accuracy is extreme. Hundreds of thousands of electronic structure calculations were required, making this model impractical to apply to larger systems. To practically explore the coupling between high and low frequency modes, there is a need for a model which can achieve the accuracy of the model of Hamm and Stock at a lower computational cost and without relying on the assumptions of the model of Myshakin et al.

1.3.2 Protonated Water Clusters

Perhaps one of the most common solutes in an aqueous solution is the hydronium ion, H_3O^+. H_3O^+ is formed when water interacts with an acid, and as such is involved in a wide array of chemical processes. However, despite its importance, there is still much to learn about the solvation shell of H_3O^+ in water. This has motivated wide array of research into protonated water clusters: gas-phase clusters consisting of one or more H_3O^+ ions bound to various numbers of water molecules. Using the experimental techniques outlined above, it is possible to create protonated water clusters of virtually any size.

Early work in protonated water clusters began in the 1960s and 1970s[21–23]. One of the early aims of protonated water clusters was to determine the basic solvation of H^+ in water[24]. Two primary structures for the hydration of a proton had previously been proposed for bulk water: the first is the "Eigen" structure, where the proton is strongly bound to a single water molecule, forming a hydronium (H_3O^+) ion[25]. The second is the "Zundel" structure, where the proton is shared between two oxygen atoms[26]. This delocalization of the bond creates a substantial red shifting in the vibrational frequency compared to a standard OH stretch. This is difficult to measure in bulk water, but can easily be seen in a gas-phase cluster[27]. However, as research into protonated water clusters progressed, it became clear that the solvation of a proton is extremely complex with a large variety of configurations, including variations of both Eigen and Zundel structures[28]. Unfortunately, in gas-phase clusters, these structures are highly dependent on the number of water molecules in the cluster, making it impossible to conclusively assign the structure of a cluster to bulk water. Despite this limitation, data from protonated water clusters continues to provide invaluable insight into the nature of a solvated proton.

One early observation was the relative stability of different sizes of protonated water clusters, measured using the relative prevalence of different clusters in a mass spectrometer. As the size of the clusters increases, their prevalence tends to decrease. However, there are a few outliers, one of the most notable being $H_3O^+ \cdot (H_2O)_{20}$, or ${W_{21}}^+$[23, 24, 29]. This cluster is more prevalent than both ${W_{20}}^+$ and ${W_{22}}^+$. There was much interest in finding the structure of ${W_{21}}^+$ to understand why this cluster was particularly stable. After much debate, a combination of experimental and theoretical techniques determined that ${W_{21}}^+$ consists of a dodecahedral cage surrounding a single water monomer[29, 30]. Notably, the H_3O^+ ion is a part of the cage structure, and not on the inside. While the basic structure of ${W_{21}}^+$ is known, there are still unanswered questions about the exact bonding arrangement of the water monomers and the pathways for conversion of one structural isomer to another.

There has been a substantial effort to bridge the gap between small water clusters and the bulk water system, aided by developments in experimental and computational techniques. Daly et al. were able to use a combination of infrared and Raman spectroscopy to determine that these spectral signatures can be predominantly attributed to Zundel and Zundel-like structures, which was aided by the extensive work on those structures in protonated water clusters[31]. Bowman and coworkers combined cluster and bulk methods by creating an accurate many-body potential energy surface for water clusters. They then used molecular dynamics simulations of bulk protonated water to generate geometry configurations of the hydrated proton. The potential energy surface could then be used to calculate anharmonic frequencies of these configurations using the geometry of just the proton and its nearest neighbors[28, 32]. In addition to this exciting work, several groups have done work on larger protonated water clusters containing 100 or 200 molecules, building upon the techniques used on smaller clusters[33, 34]. As the size of the clusters increases, their properties approach those of bulk water. New developments in mass spectrometry may soon allow these clusters to be studied at a similar level of detail as smaller clusters[35, 36].

2.0 One-Dimensional Adiabatic Model Approach for Calculating Progressions in Vibrational Spectra of Ion-Water Complexes

This paper was published in the journal Physical Chemistry C in 2018. Reprinted with permission.

Many water-anion complexes of the form $X^- \cdot (H_2O)$, where X^- is a polyatomic anion, display a peak progression in the OH stretch region of the vibrational spectra with spacings of 65-85 cm^{-1}. These progressions result from strong anharmonic coupling between the OH stretch and a low-frequency intermolecular rock vibration. In this study, we calculate these progressions in $HCO_2^- \cdot (H_2O)$, $NO_3^- \cdot (H_2O)$, and $CS_2^- \cdot (H_2O)$ by use of a one-dimensional adiabatic model with rock potentials generated from ab initio energies and frequencies. The importance of using a geometry-dependent reduced mass in calculating the peak spacings is demonstrated. We find that the one-dimensional adiabatic model is more successful in predicting peak spacings in the spectrum of $HCO_2^- \cdot (H_2O)$ than for $NO_3^- \cdot (H_2O)$, for which the rock vibration is highly anharmonic.

2.1 Introduction

The nature of ions in aqueous environments is of fundamental importance in a wide range of chemical and biological processes. One of the most powerful tools for the elucidation of the structure and dynamics of liquid water, both pure and with various solutes, is infrared vibrational spectroscopy. In aqueous solution, the spectroscopic features associated with the OH stretch vibrations of the water molecules tend to be quite broad, limiting the information that can be deduced about the H-bonding arrangements in the vicinity of dissolved ions. On the other hand, vibrational spectroscopy of cold size-selected ion-water clusters in the gas phase allows the determination of the spectroscopic signatures of well-defined bonding arrangements[13, 14, 37–40]. Even for ion-water complexes containing only a single water molecule, the vibrational spectra can be surprisingly complicated, displaying more structure than would be expected in the normal mode approximation. For example, the IR spectra of many anion-water complexes, including $CH_3CO_2^- \cdot (H_2O)$ [19], $HCO_2{}^- \cdot (H_2O)$ [14, 17, 18], $CH_3NO_2^- \cdot (H_2O)$[19], and $NO_3{}^- \cdot (H_2O)$[13], display progressions of peaks with spacings of 65-85 cm^{-1} in the OH stretch region. These progressions have been interpreted as arising from strong coupling between the OH stretch modes and the low-frequency intermolecular rock vibration[13, 14, 19, 20].

Myshakin et al. showed that the experimentally observed vibrational progressions in $CH_3CO_2{}^- \cdot (H_2O)$ and $CH_3NO_2{}^- \cdot (H_2O)$ can be qualitatively reproduced by an analytical model using a cubic coupling between the rock and OH stretch modes[19]. In recent years, this model has been used in analyzing the coupling of low and high frequency modes in several other systems[13, 18, 38, 41]. However, it assumes that the low frequency mode (the rock mode for the above complexes) is well described as harmonic and is unchanged upon excitation of an OH stretch vibration, assumptions that are not quantitatively valid for many water-anion complexes. Hamm and Stock[20] used a six-dimensional model to calculate the progression in the OH stretch region of $HCO_2{}^- \cdot (H_2O)$, achieving good agreement to experimental results. Their calculations showed that degrees of freedom other than the OH stretch and the rock vibration become important for the higher energy peaks in the progression. However, this treatment required a large number of ab initio energy evaluations, and thus, would be difficult to extend to much larger systems. We consider it valuable to establish how well an ab initio based one-dimensional model does at predicting the progressions due to rock-stretch coupling without relying on the assumptions of the model of Myshakin, et al.

In this work, we study rock-stretch coupling in anion-water clusters using an extension of the adiabatic model of Robertson et al[14]. In our application of this approach, we calculate separate rock potentials for the clusters with zero and one quanta in OH stretch, and then use these adiabatic potentials to calculate the progressions in the spectra. The equilibrium geometries of the three clusters chosen for study, $HCO_2{}^- \cdot (H_2O)$, $NO_3{}^- \cdot (H_2O)$, and $CS_2{}^- \cdot (H_2O)$, are shown in Figure 2.1. Both $HCO_2{}^- \cdot (H_2O)$ and $NO_3{}^- \cdot (H_2O)$ show progressions due to rock-stretch coupling in their vibrational spectra[13, 14, 17, 18], while $CS_2{}^- \cdot (H_2O)$ does not[14]. The rock vibration of $NO_3{}^- \cdot (H_2O)$ is highly anharmonic[13], and thus, this system provides a stringent test of reduced dimension models.

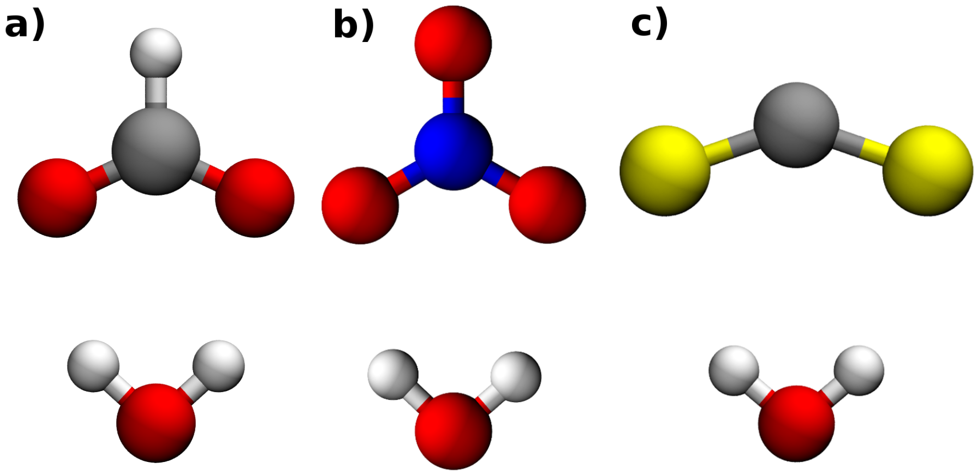

Figure 2.1: Minimum energy structures of the (a) $HCO_2{}^- \cdot (H_2O)$, (b) $NO_3{}^- \cdot (H_2O)$, and (c) $CS_2{}^- \cdot (H_2O)$ clusters.

2.2 Theoretical Methods

2.2.1 Adiabatic Model

Adiabatic models have been used to predict the vibrational spectra of a range of systems with strong coupling of low and high frequency vibrational modes[19, 20, 38, 41–45]. In this work, we build on the approach of Robertson et al.[14] to generate adiabatic rock potentials for $X^- \cdot (H_2O)$ complexes, where X^- is one of $HCO_2{}^-$, $NO_3{}^-$, or $CS_2{}^-$. To model the rock-stretch coupling, we generate separate rock potentials for $N = 0$ and $N = 1$, where N is the number of quanta of OH stretch. For each system, we start with the ab initio Born-Oppenheimer (BO) potential energy curve calculated as a function the rock angle θ, defined as the angle between the HOH bisector and the vector connecting the central atom of the anion and the water oxygen atom as illustrated in Figure 2.2. A Z-matrix was used to freeze θ while allowing all other in-plane degrees of freedom to be optimized. The $N = 0$ adiabatic potential energy curve is then generated using:

$$V_{N=0}(\theta) = E_{BO}(\theta) + ZPE(\theta) - \frac{\hbar}{2}\omega_r(\theta) \tag{1}$$

where E_{BO} is the BO energy, ZPE is the harmonic zero-point vibrational energy, and ω_r is the harmonic value of the rock frequency, all calculated as a function of θ. The $-\frac{\hbar}{2}\omega_r(\theta)$ term removes the contribution of the zero-point energy of the harmonic rock frequency. The $N = 1$ adiabatic potential is then obtained by adding the energy of one of the two OH stretch vibrations to $V_{N=0}$:

$$V_{N=1}(\theta) = V_{N=0}(\theta) + \hbar\omega_{OH}(\theta) \tag{2}$$

where ω_{OH} is calculated either in the harmonic approximation or with the inclusion of anharmonic effects (as described below in the anharmonic OH stretch section). If we simply use the energy of the lower frequency OH stretch vibration in Eq. 2 at each value of θ considered, a symmetric double-well potential would result. However, for most of this paper we make use of single-well $N = 1$ potentials. These are generated by using the energy of the lower frequency OH stretch vibration for $\theta > \theta_o$ and the energy of the higher frequency OH stretch vibration for $\theta < -\theta_o$, where θ_o is chosen to be between 1 and 2°, and interpolation is used for the intermediate θ values. This removes the discontinuity that results from the small difference in the two normal mode OH stretch frequencies at $\theta = 0$. The choice of θ_o is relatively unimportant provided a smooth interpolation is possible.

While these single-well potentials involve an adiabatic separation between the rock and OH stretch vibrations, the two OH stretch vibrations, and thus the two $N = 1$ potentials, are essentially separated diabatically. We justify this approach due to the localization of the OH stretch vibrations for non-zero θ values: the OH stretch vibrations of the complexes studied, when calculated in the normal mode approximation, are mostly localized even at θ values as small as 5 degrees in magnitude. The IR spectra are calculated by allowing for transitions from the lowest energy level in the $N = 0$ potential to various levels in the $N = 1$ potential, with the intensities being taken to be proportional to the square of the overlaps of the corresponding wavefunctions (intensities accounting for variation of the transition dipole moment are reported in the Supporting Information).

The general form of the kinetic energy operator for vibrational motion in internal coordinates involves derivatives of the reduced mass. In general, to keep the energy invariant to the choice of coordinates, the reduced mass must be defined with respect to the coordinate system used. The geometry dependence of the reduced mass is obtained using the Wilson G-

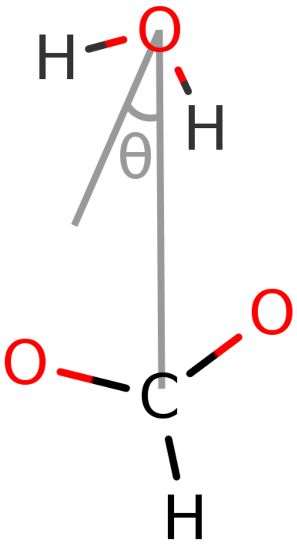

Figure 2.2: The rock angle θ of $HCO_2^- \cdot (H_2O)$, defined as the angle between the vector connecting the water oxygen and formate carbon atoms and the bisector of the water HOH angle. Similar definitions are used for $NO_3^- \cdot (H_2O)$ and $CS_2^- \cdot (H_2O)$.

matrix procedure[6, 46, 47]. For a vibration which has no kinetic coupling to other motions in the molecule, this procedure simplifies to the following equation:

$$G(q)^{-1} = \sum_{i=1}^{M} \left[\left(\frac{\partial x_i}{\partial q} \right)^2 + \left(\frac{\partial y_i}{\partial q} \right)^2 + \left(\frac{\partial z_i}{\partial q} \right)^2 \right] \tag{3}$$

where M is the number of atoms, q is the vibrational coordinate, x_i, y_i, and z_i are Cartesian coordinates of atom i, and $G(q) = 1/\mu(q)$. In normal coordinates, the atomic positions depend linearly on the coordinates and vibrational spectra can be calculated using fixed values of the reduced masses. However, for the one-dimensional adiabatic potentials employed in this study, the Cartesian coordinates vary non-linearly with θ, introducing a geometry-dependence to the reduced mass. Further details for the reduced mass calculations are given in the Supporting Information.

2.2.2 Computational Details

For each cluster, the geometry was optimized at various fixed values of the rock angle, allowing for relaxation of the other in-plane degrees of freedom. Harmonic frequency calculations were then performed for each optimized structure. For $HCO_2{}^- \cdot (H_2O)$ and $CS_2{}^- \cdot (H_2O)$, the calculations were performed using second-order Möller Plesset perturbation theory[48] with resolution of identity[49–56] (RI-MP2) in combination with the aug-cc-pVQZ basis set[57, 58]. For $NO_3{}^- \cdot (H_2O)$, the optimizations and frequency calculations were performed using explicitly correlated coupled cluster singles doubles with perturbative triples using density fitting (DF-CCSD(T)-F12)[59–63] in combination with the cc-pVDZ-F12 basis set[64] with single-point BO energies calculated at the DF-CCSD(T)-F12/cc-pVTZ-F12[64] level at the geometries optimized using the smaller basis set. The use of the CCSD(T) method rather than the MP2 method in generating the potentials for $NO_3{}^- \cdot (H_2O)$ was motivated by the fact that the rock potential of this system is highly sensitive to the theoretical method used. The $N = 0$ and $N = 1$ potential energy curves were fit to fourth and sixth order polynomials, respectively, and the vibrational energy levels were calculated using the Fourier grid Hamiltonian discrete variable representation (FGH-DVR) method[11, 12]. The RI-MP2 calculations were carried out using Turbomole 7.21[65, 66] and the DF-CCSD(T)-F12 calculations were carried out using Molpro 2018[67, 68].

2.3 Results and Discussion

In reporting the results of the calculations, we first consider the the potentials and spectra obtained using values of the OH stretch frequencies obtained using harmonic normal modes. The role of anharmonicity in the OH stretch vibrations is considered in Section 4.4. For the remainder of this paper, unless noted otherwise, harmonic OH stretch frequencies refer to those calculated using the normal mode approximation, and anharmonic OH stretch frequencies refer to those calculated using 1-D OH stretch potentials.

2.3.1 Potential Energy Curves

The $N = 0$ and $N = 1$ adiabatic rock potential energy curves for ${HCO_2}^- \cdot (H_2O)$, ${NO_3}^- \cdot (H_2O)$, and ${CS_2}^- \cdot (H_2O)$ are reported in Figure 2.3. From visual inspection it is clear that the $N = 0$ rock potentials of ${HCO_2}^- \cdot (H_2O)$ and ${CS_2}^- \cdot (H_2O)$ are more harmonic in nature than the $N = 0$ rock potential of ${NO_3}^- \cdot (H_2O)$. The coefficients of the fits to the $N = 0$ and $N = 1$ potentials of the three clusters are reported in Tables 1 and 2. For the $N = 0$ potentials, the ratio of the coefficients of the θ^4 terms to the coefficients of the θ^2 terms is greatest in magnitude for ${NO_3}^- \cdot (H_2O)$ and smallest for ${HCO_2}^- \cdot (H_2O)$. In ${NO_3}^-$, the excess charge is delocalized over three O atoms, as opposed to being delocalized over two O atoms in ${HCO_2}^-$, causing ${NO_3}^- \cdot (H_2O)$ to have a flatter rock potential than ${HCO_2}^- \cdot (H_2O)$. The origin of the steeper rock potential for ${CS_2}^- \cdot (H_2O)$ is less clear, but may be due in part to the fact that much of the excess charge of CS_2^- is localized on the C atom.

For the $N = 1$ potentials, we are especially interested in the displacements of their potential energy minima relative to those of the $N = 0$ potentials, and the degree of anharonicity of the potentials. For ${HCO_2}^- \cdot (H_2O)$ and ${NO_3}^- \cdot (H_2O)$, the $N = 1$ potential energy minima are displaced by 21.0° and 22.7°, respectively. For both of these clusters, the coefficient of the θ^2 term is much greater in the $N = 1$ potential than in the $N = 0$ potential. Moreover, for both clusters the $N = 1$ potentials have sizeable θ^3 terms with the θ^3 term being about twice as large for ${NO_3}^- \cdot (H_2O)$ as for ${HCO_2}^- \cdot (H_2O)$. For ${CS_2}^- \cdot (H_2O)$, the minimum in the $N = 1$ potential is displaced by only 4.0°, and the cubic contribution to the potential is much smaller than for $HCO_2{}^- \cdot (H_2O)$ or $NO_3{}^- \cdot (H_2O)$. This is a consequence of the fact that the variation of the OH stretch frequency with θ is much smaller for $CS_2{}^- \cdot (H_2O)$ than for $HCO_2{}^- \cdot (H_2O)$ or $NO_3{}^- \cdot (H_2O)$.

In the model Hamiltonian of Myshakin et al.,[19] the cubic anharmonic coupling term is linear in the rock coordinate, which implies that if the $N = 0$ potential is harmonic, the $N = 1$ potential is also harmonic with the same curvature. The large differences in the coefficients of the θ^2 terms between the $N = 0$ and $N = 1$ potentials for $HCO_2{}^- \cdot (H_2O)$ and $NO_3{}^- \cdot (H_2O)$ indicates the importance of anharmonic couplings that are nonlinear in the rock coordinate.

Table 2.1: Coefficients of quartic polynomial fits of the $N = 0$ potentials in $\mathbf{cm^{-1}/degree^n}$

	θ^2	θ^4
$HCO_2{}^- \cdot (H_2O)$	0.2876	8.53×10^{-6}
$NO_3{}^- \cdot (H_2O)$	0.0970	9.00×10^{-5}
$CS_2{}^- \cdot (H_2O)$	0.7992	-1.33×10^{-4}

Table 2.2: Coefficients of sextic polynomial fits of the $N = 1$ potentials in $\mathbf{cm^{-1}/degree^n}$

Cluster	θ^2	θ^3	θ^4	θ^5	θ^6
$HCO_2{}^- \cdot (H_2O)$	0.564	4.97×10^{-3}	-1.18×10^{-4}	-2.75×10^{-6}	-1.37×10^{-8}
$NO_3{}^- \cdot (H_2O)$	0.594	0.0116	-2.74×10^{-5}	-2.80×10^{-6}	-1.67×10^{-8}
$CS_2{}^- \cdot (H_2O)$	0.991	-3.65×10^{-4}	-3.03×10^{-4}	3.74×10^{-7}	5.71×10^{-8}

2.3.2 Reduced Mass

Figure 2.4 reports the reduced masses as a function of θ for the three clusters. The variation of the reduced mass with θ is largest for $HCO_2{}^- \cdot (H_2O)$ and smallest for $CS_2{}^- \cdot (H_2O)$. The reduced mass variation is largely caused by the coupling with θ of the intermonomer

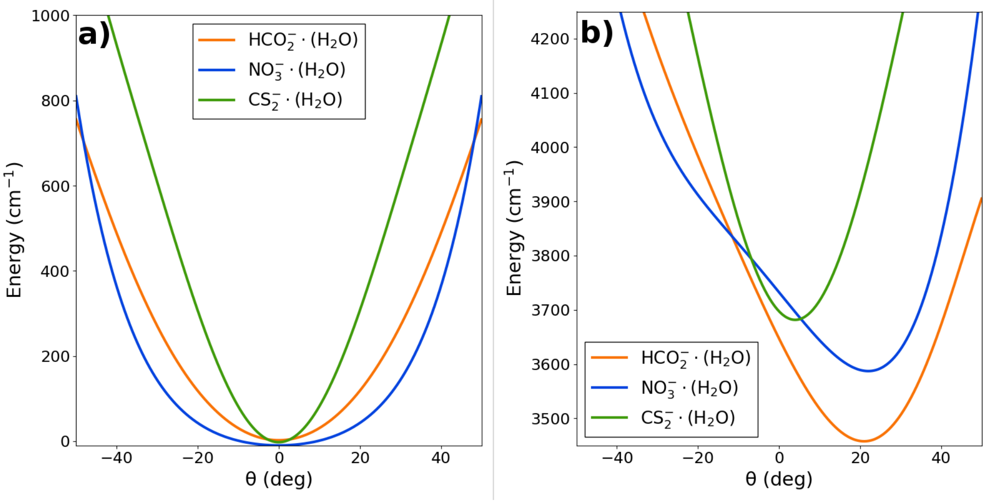

Figure 2.3: Adiabatic $N = 0$ (left) and $N = 1$ (right) potentials for $HCO_2{}^- \cdot (H_2O)$, $NO_3{}^- \cdot (H_2O)$, and $CS_2{}^- \cdot (H_2O)$. The $N = 1$ potentials have been calculated using harmonic normal mode values of the OH stretch frequencies.

separation r, which is defined as the distance between the water oxygen and the central atom of the anion, and the anion rock angle ϕ, defined in Figure 2.5a. The variation of r and ϕ with respect to θ is shown in Figures 2.5b and 2.5c. The variation of r with θ is greatest for $HCO_2{}^- \cdot (H_2O)$ and smallest for $NO_3{}^- \cdot (H_2O)$, while the change in ϕ with θ is greatest for $HCO_2{}^- \cdot (H_2O)$ but smallest for $CS_2{}^- \cdot (H_2O)$. The turnover in the reduced mass for $CS_2{}^- \cdot (H_2O)$ at θ values near ±25° is unimportant, since the relevant vibrational energy levels of the $N = 0$ and $N = 1$ potentials of this system do not significantly sample θ values larger than this in magnitude. To examine the impact of using a variable reduced mass on the calculated energy levels, we consider three reduced masses for each cluster: the reduced mass at the equilibrium geometry of the $N = 0$ potential $\mu_{eq,N=0}$, the reduced mass at the equilibrium geometry of the $N = 1$ potential $\mu_{eq,N=1}$, and μ_{var} which allows for variation of the reduced mass with θ. Tables 3, 4, and 5 report the spacings of the vibrational levels calculated for the $N = 0$ and $N = 1$ potentials of each cluster for the different choices of the reduced mass.

For the $N = 0$ potentials with $\mu_{eq,N=0}$, the spacing of successive vibrational levels is nearly

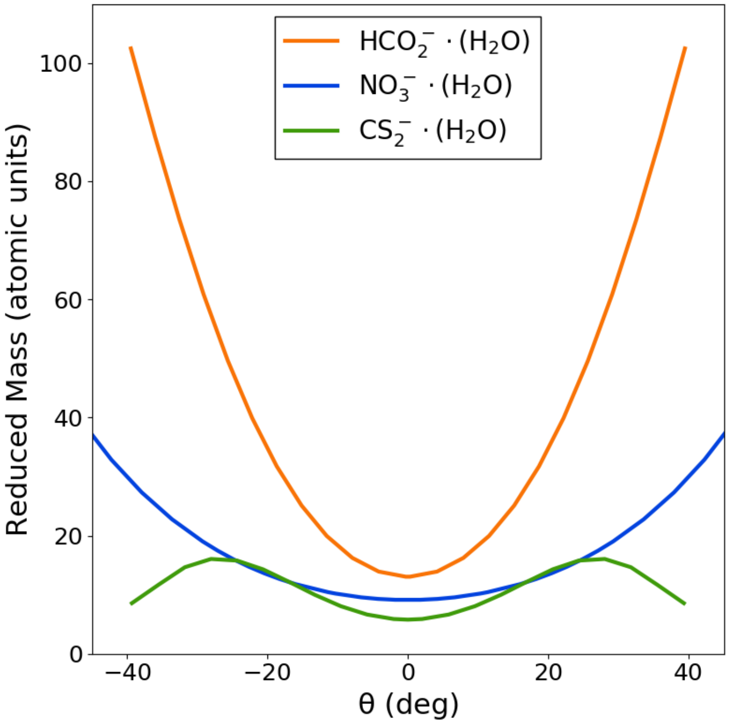

Figure 2.4: θ-dependent reduced masses for ${HCO_2}^- \cdot (H_2O)$, ${NO_3}^- \cdot (H_2O)$, and ${CS_2}^- \cdot (H_2O)$.

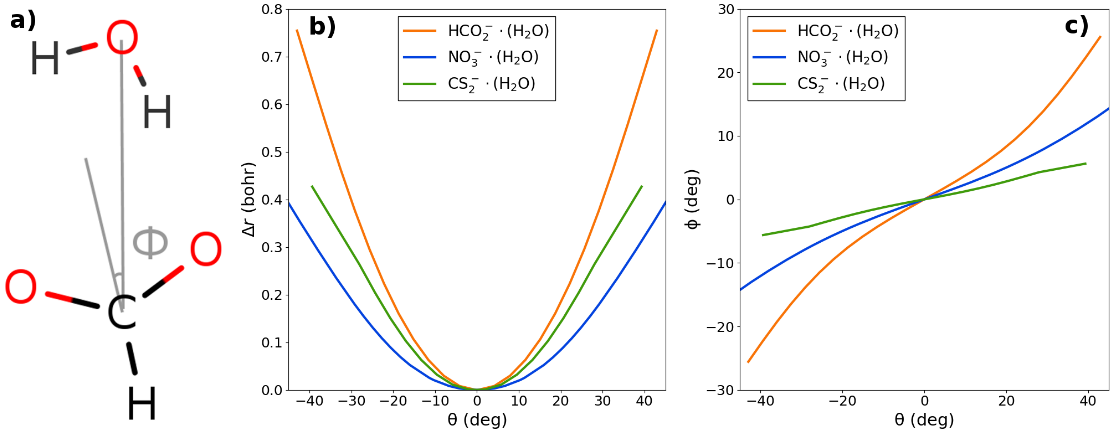

Figure 2.5: Variation of the intermolecular distance r and the anion rock angle ϕ (defined in 5a) with θ for $HCO_2{}^- \cdot (H_2O)$, $NO_3{}^- \cdot (H_2O)$, and $CS_2{}^- \cdot (H_2O)$. 5b compares the change in intermonomer distance r with respect to θ, and 5c compares the change in ϕ with respect to θ.

constant for $HCO_2{}^- \cdot (H_2O)$, but increases significantly for $NO_3{}^- \cdot (H_2O)$ and decreases significantly for $CS_2{}^- \cdot (H_2O)$. This is a consequence of sizable θ^4 dependence of the $N = 0$ rock potentials of the latter two clusters, with a positive quartic force constant for $NO_3{}^- \cdot (H_2O)$ and a negative quartic force constant for $CS_2{}^- \cdot (H_2O)$. For all three clusters, the spacings of the vibrational levels in the $N = 0$ potentials are significantly reduced upon use of the geometry-dependent reduced masses.

For all three clusters, the spacings calculated for the $N = 1$ potentials are significantly reduced upon going from $\mu_{eq,N=0}$ to μ_{var}, with the changes being greatest for $HCO_2{}^- \cdot (H_2O)$ and smallest for $CS_2{}^- \cdot (H_2O)$, which is consistent with the variations of reduced mass with θ. Interestingly, for $HCO_2{}^- \cdot (H_2O)$ and $NO_3{}^- \cdot (H_2O)$, the spacings of the vibrational energy levels calculated using $\mu_{eq,N=1}$ are nearly identical to those obtained using μ_{var}. This can be understood by the fact that the vibrationally averaged reduced masses for the $N = 1$ potentials of these clusters are close to the corresponding $\mu_{eq,N=1}$ values. The situation is different for $CS_2{}^- \cdot (H_2O)$, for which the displacement between the $N = 0$ and $N = 1$ potentials is quite small, causing $\mu_{eq,N=0}$ and $\mu_{eq,N=1}$ to be very close. As a result, for $CS_2{}^- \cdot (H_2O)$, the spacings calculated using $\mu_{eq,N=1}$ are appreciably larger than those calculated using μ_{var}.

Table 2.3: Calculated spacings of the vibrational levels of the $N = 0$ and $N = 1$ potentials of $HCO_2^- \cdot (H_2O)$ in cm^{-1}.

Levels	$N = 0$, $\mu_{eq,N=0}$	$N = 0$, μ_{var}	$N = 1$, $\mu_{eq,N=0}$	$N = 1$, $\mu_{eq,N=1}$	$N = 1$, μ_{var}
$\Delta(0,1)$	98.4	80.0	130.0	76.9	78.7
$\Delta(1,2)$	100.0	69.2	122.4	74.3	76.1
$\Delta(2,3)$	101.1	63.8	116.2	71.6	72.7
$\Delta(3,4)$	101.3	59.7	112.5	69.0	68.7

Table 2.4: Calculated spacings of the vibrational levels of the $N = 0$ and $N = 1$ potentials of $NO_3^- \cdot (H_2O)$ in cm^{-1}.

Levels	$N = 0$, $\mu_{eq,N=0}$	$N = 0$, μ_{var}	$N = 1$, $\mu_{eq,N=0}$	$N = 1$, $\mu_{eq,N=1}$	$N = 1$, μ_{var}
$\Delta(0,1)$	95.8	82.6	136.7	106.8	112.0
$\Delta(1,2)$	105.4	81.9	122.7	97.0	102.3
$\Delta(2,3)$	114.2	82.3	119.6	91.1	92.9
$\Delta(3,4)$	118.1	82.9	121.9	90.4	88.3

Table 2.5: Calculated spacings of the vibrational levels of the $N = 0$ and $N = 1$ potentials of $CS_2^- \cdot (H_2O)$ in cm^{-1}.

Levels	$N = 0$, $\mu_{eq,N=0}$	$N = 0$, μ_{var}	$N = 1$, $\mu_{eq,N=0}$	$N = 1$, $\mu_{eq,N=1}$	$N = 1$, μ_{var}
$\Delta(0,1)$	238.0	198.1	258.3	245.6	215.2
$\Delta(1,2)$	224.3	168.1	238.3	227.6	181.7
$\Delta(2,3)$	212.3	156.6	222.6	212.3	165.6

2.3.3 Calculated Spectra

Figure 2.6 reports the vibrational spectra calculated for the three clusters using μ_{var} for both $N = 0$ and $N = 1$. The spectra are plotted with Lorentzian linewidths of 20 cm^{-1} to approximate the linewidths in the experimental spectra, which are included for reference for $HCO_2^- \cdot (H_2O)$[18] and $NO_3^- \cdot (H_2O)$[13]. The experimental spectrum of $CS_2^- \cdot (H_2O)$, not pictured, has a single intense peak at 3488 cm^{-1}.[14] For $HCO_2^- \cdot (H_2O)$, the calculated (0,1), (1,2), and (2,3) peak spacings are 79, 76, and 73 cm^{-1}, respectively, in excellent agreement with experiment. For $NO_3^- \cdot (H_2O)$, the corresponding calculated peak spacings are 112, 103 and 93 cm^{-1}, which are larger and more variable than the experimental spacings of about 80 cm^{-1} (The first two peaks in the experimental spectrum are split by 35 cm^{-1} and are a result of a resonance with the water bend overtone[13], which is not accounted for in our model. We assume in our analysis that the energy of the first transition is an average of the energy of the two peaks). Presumably, the poorer performance of the one-dimensional adiabatic model approach for $NO_3^- \cdot (H_2O)$ than for $HCO_2^- \cdot (H_2O)$ is due in part to the greater anharmonic nature of its BO rock potential. For $HCO_2^- \cdot (H_2O)$ and $NO_3^- \cdot (H_2O)$, the calculations give progressions with eight and four peaks with sizable intensity, respectively. While the progression length from the calculations is consistent with that observed experimentally for $NO_3^- \cdot (H_2O)$, the calculated progression is longer for $HCO_2^- \cdot (H_2O)$ than that observed experimentally. For $CS_2^- \cdot (H_2O)$, the calculations give two peaks with sizable intensity, with the intensity of the second peak being about one tenth that of the first peak. Only a single peak is seen in the experimental vibrational spectrum of $CS_2^- \cdot (H_2O)$[14]. The origins of the calculated progressions begin at 3450, 3630, and 3688 cm^{-1} for $HCO_2^- \cdot (H_2O)$, $NO_3^- \cdot (H_2O)$, and $CS_2^- \cdot (H_2O)$, respectively. These are 200-300 cm^{-1} higher than the experimental progression origins. This is not surprising, since harmonic OH stretch frequencies were used in generating the $N = 1$ adiabatic potentials. We investigate the impact of using anharmonic OH stretch frequencies in constructing the $N = 1$ potentials in the next section.

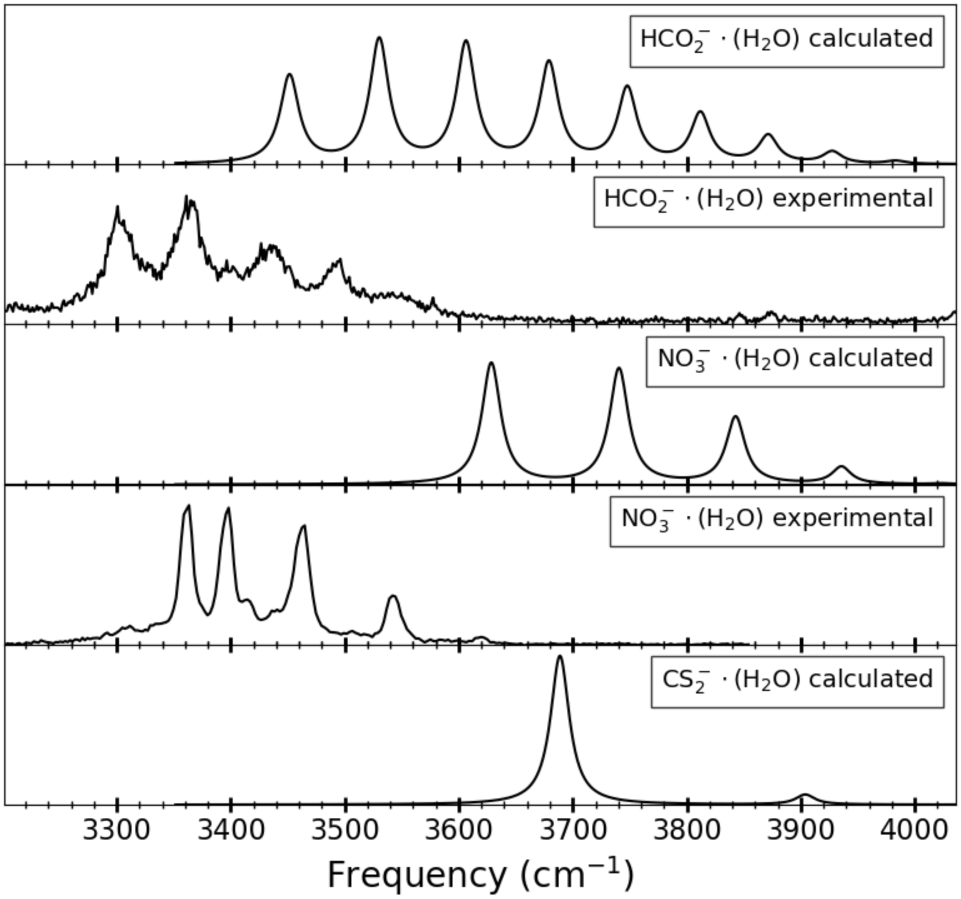

Figure 2.6: OH stretch vibrational spectra of $HCO_2{}^- \cdot (H_2O)$, $NO_3{}^- \cdot (H_2O)$, and $CS_2{}^- \cdot (H_2O)$. The calculated spectra were obtained using adiabatic potentials based on harmonic frequencies. Experimental $NO_3{}^- \cdot (H_2O)$ and $HCO_2{}^- \cdot (H_2O)$ spectra are from references 5 and 9, respectively.

2.3.4 Anharmonic OH stretch

The adiabatic potentials reported in the previous section were calculated using unscaled harmonic OH stretch frequencies. In general, OH stretching frequencies are overestimated in the harmonic approximation. To address this, for $HCO_2^- \cdot (H_2O)$ and $NO_3^- \cdot (H_2O)$, starting at the optimized geometry at each value of θ considered, we generated one-dimensional OH stretch potentials by calculating the BO energy at the RI-MP2/aug-cc-pVQZ level of theory over a range of positions of the H atom displaced along the OH bond vector. The resulting potentials were fit to sixth-order polynomials, and the OH stretch vibrational energy levels were calculated using the FGH-DVR method with constant reduced masses of 0.992 amu and 0.995 amu for $HCO_2^- \cdot (H_2O)$ and $NO_3^- \cdot (H_2O)$, respectively. The use of constant reduced masses is justified because the Cartesian atomic positions vary linearly with the OH bond length, and the specific values of the reduced mass are consistent with the G-Matrix procedure described previously. For $HCO_2^- \cdot (H_2O)$, the 1-D anharmonic OH stretch frequency as a function of θ was used directly in Equation 2 to calculate the $N = 1$ potential. Because different electronic structure methods were used to calculate the 1-D OH stretch potential and the $N = 0$ adiabatic rock potential of $NO_3^- \cdot (H_2O)$, the differences between the normal mode harmonic frequency and the 1-D anharmonic frequency, both calculated using the RI-MP2 method, were added to the previously used DF-CCSD(T) frequency at each θ value considered to obtain anharmonic values of $\omega_{OH}(\theta)$. Inclusion of vibrational anharmonicity of the OH stretch vibrations in the zero-point energy was found to be relatively unimportant for the calculated energy levels and was therefore neglected.

The $N = 1$ potentials obtained using harmonic and anharmonic OH stretch frequencies are compared in Figure 2.7, and the spectra obtained using the two sets of potentials are shown in Figure 2.8. For both clusters, inclusion of anharmonicity in the OH strech frequency leads to small increases in the calculated peak spacings (a few wavenumbers). However, the progression origins decrease dramatically, down to 3032 cm^{-1} for $HCO_2^- \cdot (H_2O)$ and to 3275 cm^{-1} for $NO_3^- \cdot (H_2O)$. Thus, the approach used to include the effects of anharmonicity overcorrects the progression origin of $NO_3^- \cdot (H_2O)$ by about 100 cm^{-1} and $HCO_2^- \cdot (H_2O)$ by over 200 cm^{-1}. This overcorrection is most likely due to the fact that the model does not

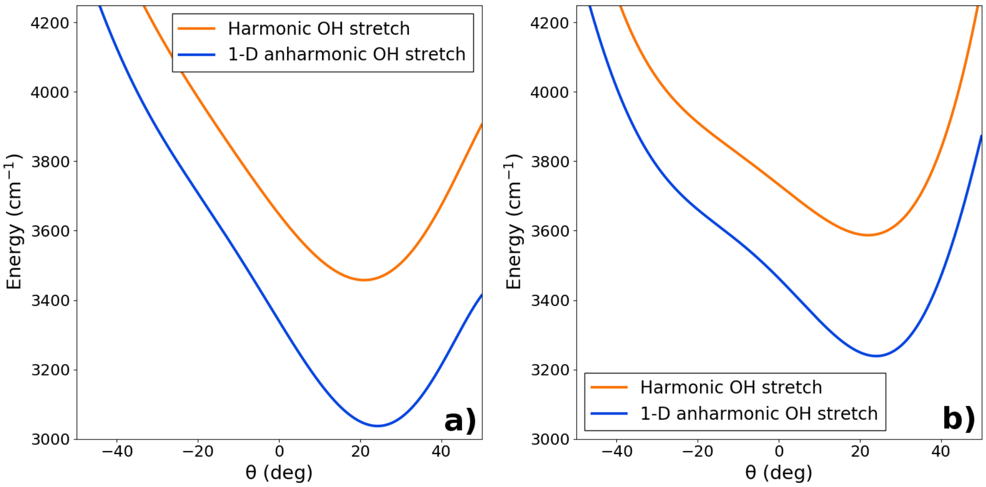

Figure 2.7: Comparison of the $N = 1$ rock potentials generated using harmonic and anharmonic OH stretch frequencies for (a) $HCO_2{}^- \cdot (H_2O)$ and (b) $NO_3{}^- \cdot (H_2O)$.

account for coupling between the OH stretch and other modes or overtone and combination bands. It appears that in order to obtain accurate progression origins, a higher dimensional anharmonic model than used here will be required.

We also generated 1-D OH stretch potentials retaining only the quadratic terms in the potentials and used these to calculated pseudo-harmonic OH stretch frequencies. These frequencies were 75-85 cm^{-1} lower than those obtained from the normal mode calculations of the full clusters. These frequency shifts are considerably smaller than those obtained using the energy levels of the anharmonic 1-D potentials.

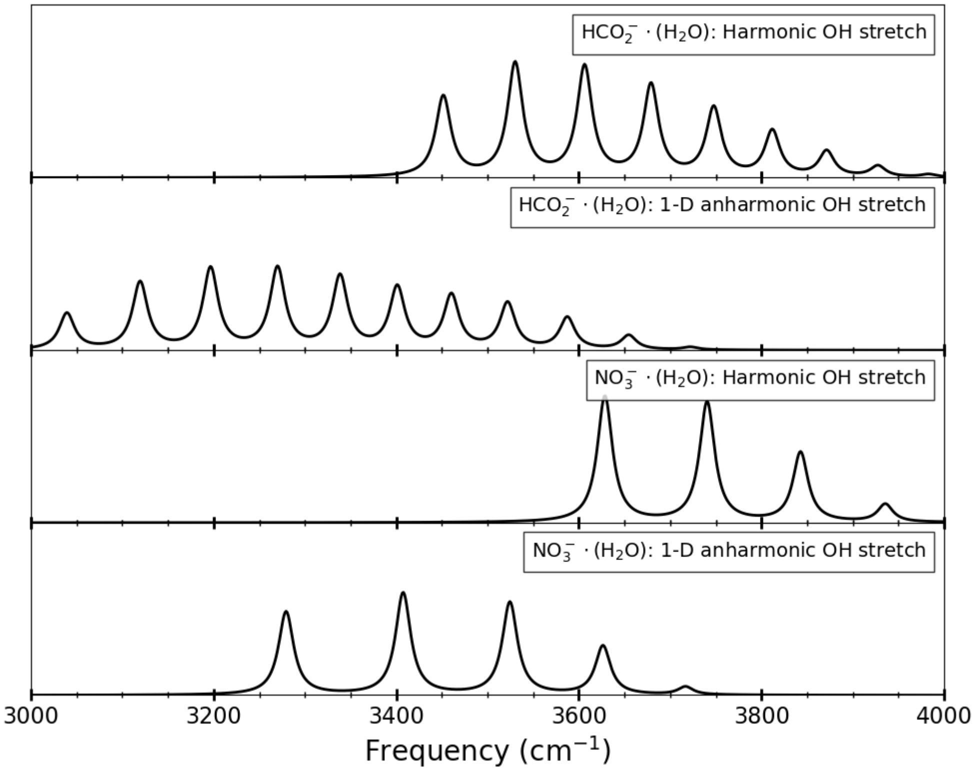

Figure 2.8: Comparison of the spectra calculated using $N = 1$ potentials generated with harmonic and anharmonic OH stretch frequencies for $HCO_2{}^- \cdot (H_2O)$ and $NO_3{}^- \cdot (H_2O)$.

2.3.5 Double-well $N = 1$ potentials

The single-well $N = 1$ potentials used in the previous sections of the paper ignored mixing between the two local OH stretch motions that occur in the normal-mode approximation and which is most important near $\theta = 0$. As a result, these potentials are essentially diabatic representations with respect to the OH stretch vibrations. In this section, we investigate how the calculated vibrational spectra of $HCO_2^- \cdot (H_2O)$ and $NO_3^- \cdot (H_2O)$ are impacted when allowing for the double-well character of the fully adiabatic $N = 1$ potentials. The double-well potentials are generated using:

$$V^- = 1/2(V_1 + V_2) - 1/2\sqrt{(V_1 - V_2)^2 + 4W^2} \tag{4}$$

where V_1 and V_2 are the original single-well $N = 1$ potentials and the coupling W is taken to be a constant equal to one-half the difference in the two harmonic OH stretch frequencies at $\theta = 0$. We note that this procedure gives nearly identical double-well potentials as simply choosing the lower OH stretch frequency at each θ value when harmonic normal mode frequencies are used. The advantage of using Equation 4 is that it can also be used with anharmonic values of the OH stretch energies generated from the 1-D potentials described in the previous section.

Figure 2.9 shows the $N = 1$ double-well potentials for $HCO_2^- \cdot (H_2O)$ and $NO_3^- \cdot (H_2O)$ calculated using Equation 4. We generate double-well potentials in conjunction with both harmonic normal mode OH stretch frequencies and anharmonic OH stretch frequencies calculated from 1-D potentials. The values for W used were 0.65 cm^{-1} for $HCO_2^- \cdot (H_2O)$ and 4.57 cm^{-1} for $NO_3^- \cdot (H_2O)$. The vibrational energy levels obtained from calculations using these potentials and geometry-dependent reduced masses are reported in Tables 6 and 7.

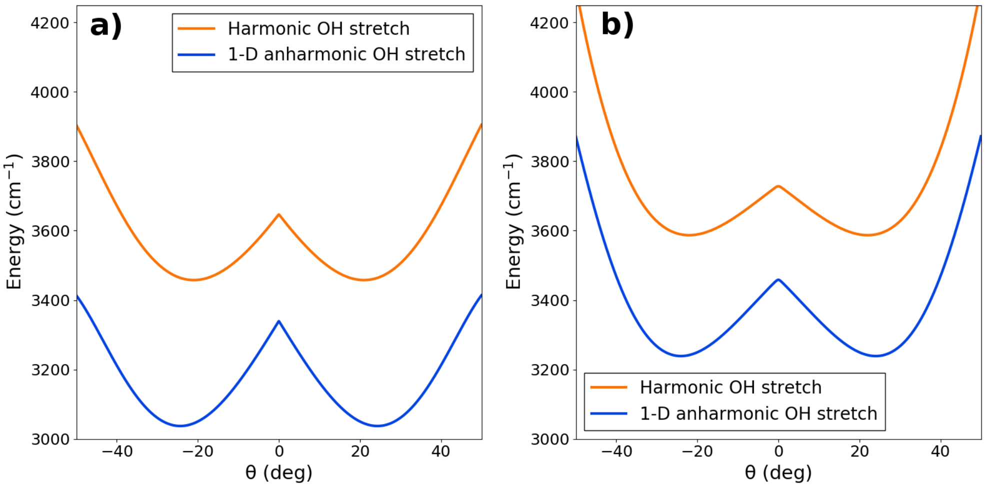

Figure 2.9: Double-well potentials of (a) $HCO_2^- \cdot (H_2O)$ and (b) $NO_3^- \cdot (H_2O)$ obtained using Equation 4.

Table 2.6: Energy levels (cm^{-1}), relative intensities, and spacings (cm^{-1}) for the double-well *N = 1* potential of $HCO_2^- \cdot (H_2O)$

	Harmonic OH stretch[a]			Anharmonic OH stretch[b]		
Levels	Energy	Intensity	Spacing	Energy	Intensity	Spacing
0	35.8	0.33	-	44.0	0.14	-
1	107.8	0.40	72.0	122.0	0.27	78.0
2	179.6	0.19	71.9	194.1	0.29	72.1
3	257.4	0.06	77.8	263.3	0.17	69.2
4	337.5	0.02	80.2	333.1	0.02	66.5

[a]: These results were obtained using the orange potential shown in Figure 9a

[b]: These results were obtained using the blue potential shown in Figure 9a

For $HCO_2^- \cdot (H_2O)$, the spacings in the spectra calculated using the double-well potentials are roughly the same as those obtained using the single-well potentials (agreeing to within 10% for the first three spacings). However, the peak progressions calculated using

Table 2.7: Energy levels (cm^{-1}), relative intensities, and spacings (cm^{-1}) for the double-well *N = 1* potential of $NO_3^- \cdot (H_2O)$

	Harmonic OH stretch[a]			Anharmonic OH stretch[b]		
Levels	Energy	Intensity	Spacing	Energy	Intensity	Spacing
0	73.3	0.74	-	81.8	0.54	-
1	177.8	0.23	104.6	191.7	0.38	109.9
2	316.3	0.03	138.4	320.5	0.07	128.7
3	475.1	0.00	158.8	475.4	0.01	154.9

[a]: These results were obtained using the orange potential shown in Figure 9b

[b]: These results were obtained using the blue potential shown in Figure 9b

the double-well potentials are much shorter, with only four transitions predicted to carry significant intensity. This agrees well with the experimental spectrum, where only four peaks are visible.

For $NO_3^- \cdot (H_2O)$, the spacing between the first two peaks in the spectrum calculated using the double-well potentials are similar to those obtained using the single-well potentials. However, the spacings between subsequent peaks are even more overestimated compared to experiment than those calculated using the single-well $N = 1$ potential. The use of the double-well potentials also leads to shortened progressions in the calculated vibrational spectrum of $NO_3^- \cdot (H_2O)$, with only two and three peaks being calculated to have sizable intensity when using harmonic and anharmonic OH stretch frequencies, respectively. The latter result is consistent with the number of peaks visible in experiment (after "removing" the extra peak that appears due to resonance with the water bend overtone).

2.4 Conclusions

Progressions of peaks in the OH stretch region are seen in the IR spectra of several water-anion complexes. Qualitatively, this can be understood in terms of anharmonic coupling between the OH stretch and the intermolecular rocking modes. In this work, we explore the utility of one-dimensional adiabatic models for describing these progressions. Specifically, we generated relaxed adiabatic rock potentials for $HCO_2^- \cdot (H_2O)$, $NO_3^- \cdot (H_2O)$, and $CS_2^- \cdot (H_2O)$ with zero or one quanta of OH stretch. The resulting potentials were used to calculate the OH stretch spectra. For $CS_2^- \cdot (H_2O)$, our model gave one strong and one very weak peak, consistent with experiment from which only a single peak is seen in the OH stretch region. For $HCO_2^- \cdot (H_2O)$ and $NO_3^- \cdot (H_2O)$, which do exhibit progressions experimentally, we found that agreement with the experimental peak spacing dramatically improved when variable reduced masses obtained form the Wilson G-matrix procedure was employed. With a variable reduced mass, the calculated peak spacings for $HCO_2^- \cdot (H_2O)$ are about 15 cm^{-1} larger than those observed experimentally, while the overestimation of the spacings was larger for $NO_3^- \cdot (H_2O)$.

Treating vibrational anharmonicity in molecules and clusters with strong anharmonic couplings remains a challenging theoretical problem. The adiabatic model presented and applied in this study can provide a semiquantitatively accurate descrption of the progressions that arise in the case of strong coupling between low and high frequency modes, while having only modest demands in terms of the required electronic structure calculations. Our results suggest the need to systematically explore the applicability of higher-dimensional adiabatic models to the vibrational spectra of clusters such as $NO_3^- \cdot (H_2O)$.

The use of double-well rather than single-well $N = 1$ potentials results in progression lengths in much better agreement with experiment. This is a consequence of the energy levels above the barrier having very low intensity. However, the use of the double-well potentials while not having a major impact on the peak spacings of $HCO_2^- \cdot (H_2O)$, worsens the agreement with the experimental peak spacings in the case of $NO_3^- \cdot (H_2O)$. This is further evidence of the need to go beyond a one-dimensional treatment for $NO_3^- \cdot (H_2O)$ within the context of a reduced dimension adiabatic model.

2.5 Acknowledgements

The work in this work was supported by the United States Department of Energy under grant DE-FG02-00ER15066. Computational resources were provided by the University of Pittsburgh's Center for Research Computing. We also acknowledge Prof. Mark Johnson and Joanna Denton of Yale University for providing us with experimental data for $HCO_2^- \cdot (H_2O)$ and for valuable discussions.

3.0 Two-Dimensional Adiabatic Model for Calculating Progressions Resulting from Stretch-Rock Coupling in Vibrational Spectra of Anion-Water Complexes

This paper was published in the Journal of Physical Chemistry Letters in 2021. Reprinted with permission.

Several anion-water dimers feature a distinct progression in the OH stretch region of their vibrational spectra. This progression arises from strong anharmonic couplings between the OH stretch and low frequency intermolecular modes. In this work, we introduce a two-dimensional adiabatic model accounting explicitly for the water and anion rock degrees of freedom and use it to calculate the vibrational spectra of $HCO_2{}^- \cdot (H_2O)$ and $NO_3{}^- \cdot (H_2O)$. The spectra calculated using this model are in excellent agreement with experiment, both in terms of peak spacings and lengths of the progressions and represent a substantial improvement over earlier models.

Ion-water interactions are of fundamental importance in chemistry and biology. Vibrational spectroscopy of ions complexed with one or more water molecules has proven invaluable at elucidating the bonding arrangements at play. However, interpreting the spectra is often challenging due to the large spectral shifts and extra bands that appear due to anharmonicity. Even in the case of ion complexes with a single water molecule the vibrational spectra can deviate appreciably from the predictions of a harmonic treatment. For example, the vibrational spectra of the $NO_3{}^- \cdot (H_2O)$[13, 14], $CH_3CO_2{}^- \cdot (H_2O)$[19], $CH_3NO_2{}^- \cdot (H_2O)$[19], and $HCO_2{}^- \cdot (H_2O)$[14, 17] complexes exhibit progressions of peaks in the OH stretch region with spacings of 60-80 cm^{-1}. The simplest theoretical model for treating this structure is that of Myshakin et al.[19], which employs only the two OH stretch vibrations and the low-frequency intermolecular rocking mode as well as their coupling through a single cubic coupling term in the Hamiltonian. Using this reduced dimension Hamiltonian, Myshakin et al. obtained simple analytical expressions for the frequencies and intensities by applying a Born-Oppenheimer (BO) like separation between the high-frequency OH stretch vibrations and the low-frequency intermolecular (IM) rock vibration. This approach was used to calculate the spectra of $CH_3NO_2{}^- \cdot (H_2O)$ and $CH_3CO_2{}^- \cdot (H_2O)$, but it was necessary to scale the cubic coupling force constants to obtain peak spacings in good agreement with experiment. This model gave progressions much longer than those observed experimentally and also was less successful for $NO_3^- \cdot (H_2O)$ which has a more highly anharmonic BO potential energy surface[13].

In a previous study, we applied an alternative adiabatic model employing separate one-dimensional IM potential energy curves for the cluster with zero and one quanta of OH stretch[**henderson2019one**] to calculate the vibrational spectra of $HCO_2^- \cdot (H_2O)$ and $NO_3^- \cdot (H_2O)$. In this model the adiabatic potential energy curves were generated following the approach of Robertson et al.[14]. While the resulting spectra were in qualitative agreement with experiment, the peak spacings were overestimated by about 15 and 40% for $HCO_2^- \cdot (H_2O)$ and $NO_3^- \cdot (H_2O)$, respectively, and the calculated progressions were much longer than those observed experimentally, as was the case for the model of Myshakin et al. This leads us to question the suitability of one-dimensional models for treating the progressions in the vibrational spectra of these complexes.

In the water-anion clusters of interest, there are two in-plane intermolecular rock modes that can be described by the coordinates θ and ϕ, depicted in Figure 3.1. The two associated normal modes involve combinations of θ and ϕ. In our previous study, θ was scanned and all other coordinates, including ϕ, were allowed to relax. The relaxed values of ϕ were highly θ-dependent, leading us to anticipate that explicitly accounting for both coordinates could prove to be important for characterizing these progressions. This observation motivates the present study in which we explore a two-dimensional (2D) model in which both θ and ϕ are scanned. We test this 2D model by applying it to the $HCO_2^- \cdot (H_2O)$ and $NO_3^- \cdot (H_2O)$ clusters.

In this work, we construct adiabatic potentials as a function of the two angles shown in Figure 3.1. θ is defined as the angle between the HOH bisector and $\overrightarrow{r}$, the vector between the water oxygen atom and the central atom of the anion (i.e., the C atom of HCO_2^- or the N atom of NO_3^-). ϕ is defined as the angle between $\overrightarrow{r}$ and the bisector of the anion angle depicted in the figure.

We scan along a two-dimensional grid of (θ,ϕ) values, optimizing the remaining degrees of freedom, as described below. At each grid point, we calculate the harmonic vibrational

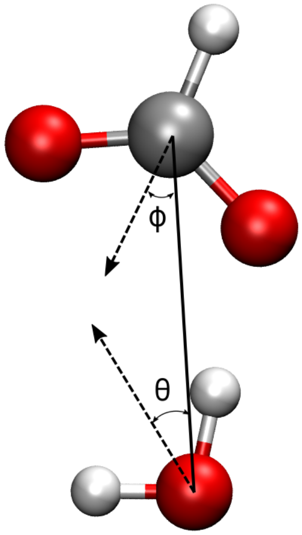

Figure 3.1: Definition of the angles θ and ϕ for $HCO_2{}^- \cdot (H_2O)$. Similar definitions are used for $NO_3{}^- \cdot (H_2O)$.

frequencies. Using these results, we generate $V_{N=0}$ and $V_{N=1}$ potential energy surfaces:

$$V_{N=0}(\theta,\phi) = E_{BO}(\theta,\phi) + ZPE(\theta,\phi) \tag{5}$$

$$V_{N=1}(\theta,\phi) = V_{N=0}(\theta,\phi) + \hbar\omega_{OH}(\theta,\phi) \tag{6}$$

where N denotes the number of quanta of OH stretch, E_{BO} is the total energy in the BO approximation, ZPE is a modified vibrational zero-point energy, and ω_{OH} is an OH stretch frequency. The normal modes for the OH stretches do not significantly mix with other motions, and are highly localized onto a single OH bond at even small deviations from ($\theta = 0, \phi = 0$). The normal mode frequencies for the OH stretch were chosen for ease of calculation; however, one could choose to use local modes and achieve similar results. For the ZPE correction, we exclude the three in-plane intermolecular vibrations, all of which have substantial contributions from both θ and ϕ.

Since the complexes have two water OH stretch vibrations, we are faced with the problem of choosing the appropriate ω_{OH} value to use in generating $V_{N=1}$. To address this problem, we employ:

$$V_{N=1}(\theta,\phi) = V_{N=0}(\theta,\phi) + \frac{\hbar}{2}\left(\omega_1(\theta,\phi) + \omega_2(\theta,\phi)\right) - \frac{\hbar}{2}\sqrt{\left(\omega_1(\theta,\phi) - \omega_2(\theta,\phi)\right)^2 + 4W^2} \quad (7)$$

where ω_1 and ω_2 are the two OH stretch frequencies and W is one-half of the splitting between the two frequencies at $\theta = 0$ and $\phi = 0$. Additionally, both ω_1 and ω_2 are scaled by 0.954 to account qualitatively for diagonal anharmonicity. The scale parameter was chosen to bring the calculated harmonic OH stretch frequency of the isolated HOD molecule into agreement with experiment.

The potential energy surfaces of $HCO_2^- \cdot (H_2O)$ and $NO_3^- \cdot (H_2O)$ were calculated over two-dimensional grids with $-70 \leq \theta \leq 70$ and $-50 \leq \phi \leq 50$, with five degree increments for each angle. At each grid point, all remaining in-plane degrees of freedom were optimized using second-order Möller-Plesset perturbation theory[48, 63] with density fitted integrals (DF-MP2)[49, 50, 52–56] and the aug-cc-pVTZ basis set[57, 58]. The harmonic frequencies were calculated at the same level of theory. The optimization and harmonic frequency calculations were performed using Molpro 2018[67–69], and the vibrational energy levels and wavefunctions for the resulting potentials were calculated using a two-dimensional Fourier grid Hamiltonian discrete variable representation (FGH-DVR) approach[11, 12]. 2D splines were used to interpolate points from the electronic structure calculations Because the model described above employs a relaxed scan over internal coordinates, coordinate-dependent reduced masses calculated using the Wilson G-matrix are required to evaluate kinetic energy contributions[6, 7]..

Figure 3.2 shows contour plots for the adiabatic $N = 0$ and $N = 1$ 2D potential energy surfaces of $HCO_2^- \cdot (H_2O)$ and $NO_3^- \cdot (H_2O)$. The global minimum of the $HCO_2^- \cdot (H_2O)$ $N = 0$ potential occurs at $\theta = 0$, $\phi = 0$. However, for $NO_3^- \cdot (H_2O)$, there is a small barrier of 10 cm^{-1} at $\theta = 0$, $\phi = 0$, with the minima appearing near $(\theta, \phi) = (-20°, -7°)$ and $(20°, 7°)$. Previous studies of this cluster have shown that this barrier is eliminated when more accurate electronic structure methods are used, and the true global minimum occurs

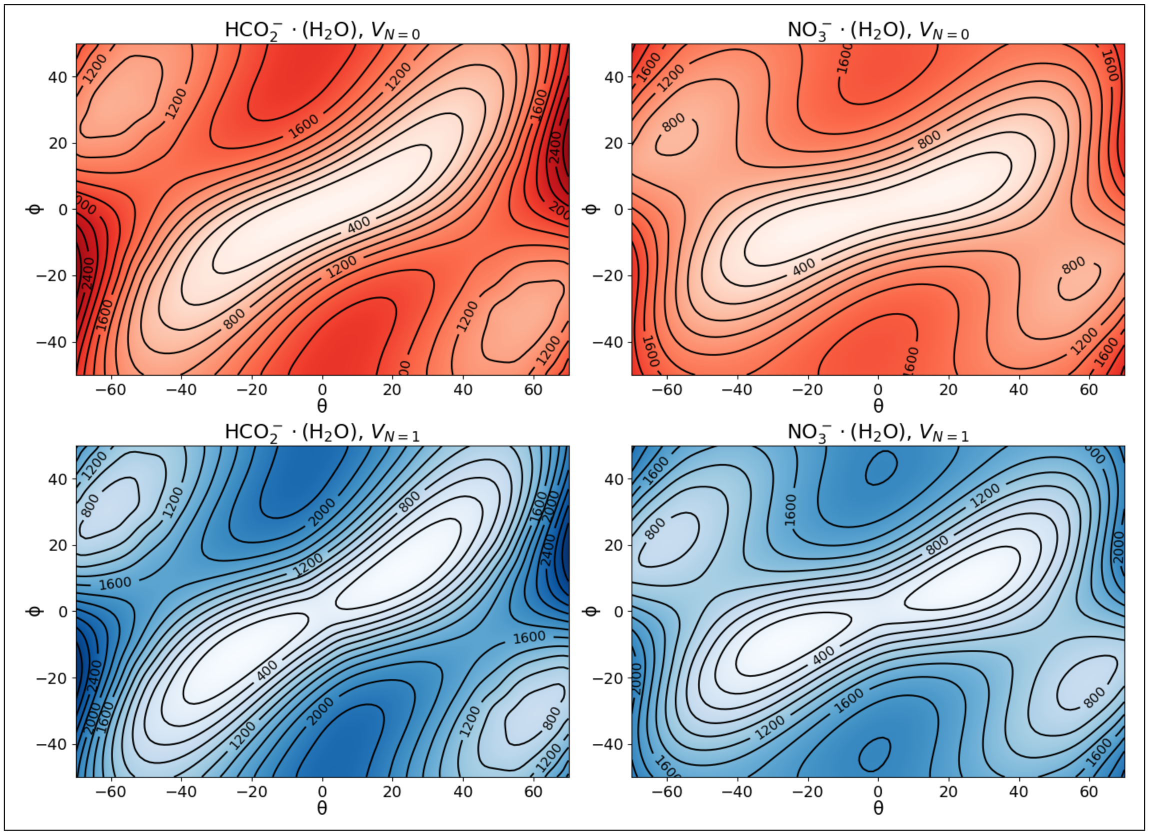

Figure 3.2: Contour plots for the 2D $V_{N=0}$ and $V_{N=1}$ potential energy surfaces of $HCO_2^- \cdot (H_2O)$ and $NO_3^- \cdot (H_2O)$. Contour levels are spaced 200 cm^{-1} apart. The minimum of each potential is set to 0 cm^{-1}.

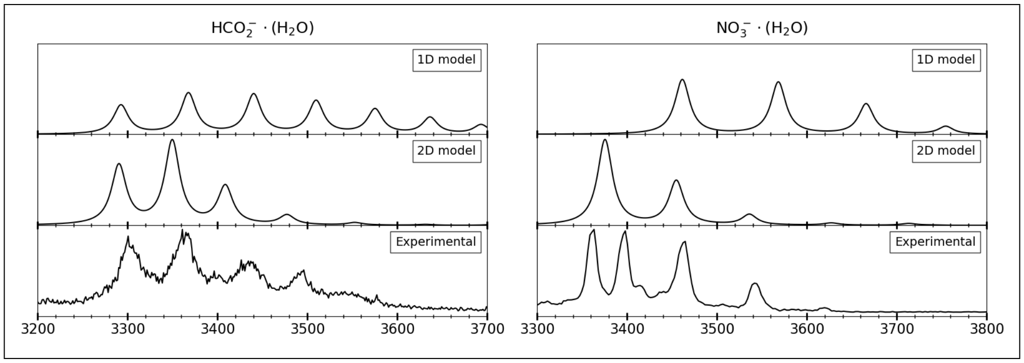

Figure 3.3: Calculated and experimental[13, 17] vibrational spectra for $HCO_2{}^- \cdot (H_2O)$ (left) and $NO_3{}^- \cdot (H_2O)$ (right). Calculated spectra from both the present 2D model and our earlier 1D model are reported.

at $\theta = 0$, $\phi = 0$[13]. Because the height of the barrier is much lower than the lowest rock energy level in this cluster, it does not have an appreciable impact on the calculated spectra.

The $N = 0$ potentials of both clusters have additional local minima near $(\theta, \phi) = (-55°, 40°)$ and $(55°, -40°)$. At these geometries, one OH group of the water molecule is essentially free and the other is hydrogen bonded to an oxygen atom of the anion. The additional minima are over 1100 cm^{-1} higher in energy than the global minima. These large-angle high energy local minima in the $N = 0$ potentials translate into additional local minima on the $N = 1$ potential energy surfaces, but these regions are not significantly sampled upon vibrational excitation from the zero-point level of the $N = 0$ potentials and thus have a negligible effect on the calculated spectra. In the low-energy region, the $N = 1$ potentials of both $HCO_2{}^- \cdot (H_2O)$ and $NO_3{}^- \cdot (H_2O)$ are double-well in nature. The barrier between the wells is 220 cm^{-1} for $HCO_2{}^- \cdot (H_2O)$ and 271 cm^{-1} for $NO_3{}^- \cdot (H_2O)$. In addition, there is a rotation of the wells in the $N = 1$ potential compared to the $N = 0$ potential.

The vibrational spectra of the clusters were calculated using transitions from the ground state level of the $N = 0$ potentials to various levels in the $N = 1$ potentials, with the intensities of the transitions taken to be proportional to the square of the overlap of the corresponding wavefunctions. The spectra are plotted using a Lorentzian broadening with a full-width half maximum of 10 cm^{-1} to approximate the experimental peak widths. Figure 3.3 also includes spectra calculated using the previous 1D model[**henderson2019one**] as well as from experiment[13, 17]. The appearance of two low-energy peaks split by about 35 cm^{-1} in the experimental spectrum of $NO_3{}^- \cdot (H_2O)$ is a consequence of a resonance between the OH stretch fundamental and water bend overtone vibrations, a coupling not included in our model[13]. This resonance is suppressed in the spectrum of $NO_3{}^- \cdot (HOD)$[13]

For both $HCO_2{}^- \cdot (H_2O)$ and $NO_3{}^- \cdot (H_2O)$, the 1D adiabatic model overestimates the spacings between peaks (by 10 cm^{-1} and 30 cm^{-1}, respectively) and gives progressions that are much too long. For both clusters, the agreement between theory and experiment is dramatically improved in going from the 1D to the 2D adiabatic model, with the calculated peak spacings, relative intensities of the peaks, and the length of the progressions being in much better agreement with experiment. The latter improvement is due in part to the rotation of the 2D potential wells upon excitation of an OH stretch, an effect which is not present in the 1D model. We note that Hamm and Stock have treated the vibrational structure of $HCO_2{}^- \cdot (H_2O)$, using a three-dimensional adiabatic model, where the intermolecular stretch was considered in addition to the rock degrees of freedom[20]. Their treatment gives a longer vibrational progression than obtained with our 2D model. The reason for this is not clear, but there are multiple differences between the two treatments in addition to the different dimensionality of the models. These include our model using a more flexible basis set (aug-cc-pVTZ vs aug-cc-pVDZ) in calculating the BO potential energy surface and a different definition of the angles used to define the rock degrees of freedom in the two studies.

In summary, we have demonstrated that for a class of water-anion complexes, a two-dimensional adiabatic model that accounts explicitly for both in-plane intermolecular rock degrees of freedom predicts vibrational progressions in the OH stretch region of the spectra in a near quantitative agreement with experiment. Although we have focused on a particular class of water-ion complexes, there are a variety of systems where two or more low frequency modes are coupled to high frequency modes. We believe that multi-dimensional adiabatic models will be a valuable tool in gaining physical insight into these systems, and hope that our results inspire additional work in this area.

3.1 Acknowledgements

This research was supported by DOE through grant number DE-SC0021065. The calculations were carried out at the University of Pittsburgh's Center for Research Computing.

4.0 Mapping the temperature-dependent and network site-specific onset of spectral diffusion at the surface of a water cluster cage

This paper was published in the Proceedings of the National Academy of Sciences in 2020. It is a collaboration with members of the Xantheas group at University of Washington and the Johnson group at Yale University. The experimental work was performed by members of the Johnson group, and the the computational work was performed jointly by members of the Xantheas and Jordan groups. Reprinted with permission.

4.1 Significance

Water's vibrational spectrum is dynamic: The OH oscillator frequency changes spontaneously within a diffuse envelope on an ultrafast timescale. Here, we explore the mechanics that drive this "spectral diffusion" at the molecular level by following the time-dependent frequency of single OH oscillators, each embedded in a cage of 20 deuterated water molecules, as a function of temperature. These cages are isolated in the gas phase and incorporate a single, isotopically labeled OH group that can occupy many spectroscopically distinct sites. The rates of spontaneous change in the OH frequency reflect the pathways for migration of the isotopic label among these sites, which occurs on a remarkably long (approximately millisecond) timescale at the onset of large-amplitude motion near 100 K.

4.2 Introduction

We explore the kinetic processes that sustain equilibrium in a microscopic, finite system. This is accomplished by monitoring the spontaneous, time-dependent frequency evolution (the frequency autocorrelation) of a single OH oscillator, embedded in a water cluster held in a temperature-controlled ion trap. The measurements are carried out by applying two-color, infrared-infrared photodissociation mass spectrometry to the $D_3O^+ \cdot (HDO)(D_2O)_{19}$ isotopologue of the "magic number" protonated water cluster, $H^+ \cdot (H_2O)_{21}$. The OH group can occupy any one of the five spectroscopically distinct sites in the distorted pentagonal dodecahedron cage structure. The OH frequency is observed to evolve over tens of milliseconds in the temperature range (90 to 120 K). Starting at 100 K, large "jumps" are observed between two OH frequencies separated by 300 cm^{-1}, indicating migration of the OH group from the bound OH site at 3,350 cm^{-1} to the free position at 3,686 cm^{-1}. Increasing the temperature to 110 K leads to partial interconversion among many sites. All sites are observed to interconvert at 120 K such that the distribution of the unique OH group among them adopts the form one would expect for a canonical ensemble. The spectral dynamics displayed by the clusters thus offer an unprecedented view into the molecular-level processes that drive spectral diffusion in an extended network of water molecules.

Chemical systems maintain equilibrium through kinetic processes that balance the populations of reactants and products. In solution, these processes involve energy exchange with the solvent, and simulations of chemical processes in solution often involve a hierarchy of methods. For example, local interactions involving the solute and first-shell solvent molecules might be treated with accurate quantum chemical methods, while the effects of the more distant solvent are included using simpler models[70, 71]. In this report, we exploit temperature-controlled water clusters to provide a well-defined system in which to monitor the dynamic behavior of a simple reversible chemical process as a function of temperature. With the aid of theory, we identify the low-energy pathways that are associated with the onset of changes in the observed spectral patterns. Gas phase cluster ions are equilibrated through collisions with a low-pressure buffer gas and interaction with blackbody radiation in a radiofrequency ion trap, and hence can be viewed as being weakly coupled to a heat bath[72]. We specifically consider the water cluster formed upon hydration of an "excess proton" by 21 water molecules, with a representative low-energy structure[73] shown in Figure 4.1A. Note that its vibrational spectrum (Figure 4.1C) strongly resembles that of the air–water interface (cf. Figure 4.1B)[74].

4.3 Results and Discussion

The specific dynamical processes at play here are the temperature-dependent pathways for migration of a single H atom through the various distinct sites in an otherwise perdeuterated cage. This is accomplished by following how the frequency of the OH oscillator evolves in time as the temperature is systematically raised to enable large-amplitude motion of the water molecules. We specifically monitor the migration of the OH oscillator among the various spectroscopically distinct sites (labeled by different colors in the structure and spectra in Figure 4.1) in the structure after a sudden disruption of the equilibrium population distribution. That is, the steady-state populations in the various network sites, constrained by the equilibrium constant (Keq) in a thermal ensemble, are sustained through steady-state, site-to-site interconversion kinetics. We remark that these rearrangements are a cluster analog of those that drive ultrafast "spectral diffusion" in bulk and interfacial water[75–81].

Our experimental approach to measuring the spontaneous kinetic processes in clusters is motivated by the classic "T-jump" approach pioneered by Eigen in the 1950s, who demonstrated a way to determine the rates of the fast reactions that sustain a macroscopic equilibrium state. That method involved quickly displacing the system away from equilibrium and then observing the time response of the populations as a new equilibrium condition is established[82]. Here, we employ a variation of this scheme in which we remove the population in one of the sites in an ensemble of clusters held at constant temperature and observe the system moving toward the new equilibrium population distribution.

The structure displayed in Figure 4.1A is one of many distorted pentagonal dodecahedron (PD) arrangements with similar oxygen atom cages but different topologies of the extended H-bonding network (see the 10 low-lying isomers in Figure 4.5)[73, 83, 84]. We introduce a single H atom into the perdeuterated isotopologue, which is isolated and studied using photofragmentation mass spectrometry as detailed in SI Appendix, Section I. These isotopologues occur in two classes according to whether the H isotope is sequestered in the hydronium ion or resides in the surrounding neutral water cage. We are here concerned with only the $D_3O^+ \cdot (HOD)(D_2O)_{19}$ type (hereafter denoted PDOH) because the OH stretches of the embedded hydronium are known to lie near 2,000 cm^{-1} and do not contribute to the

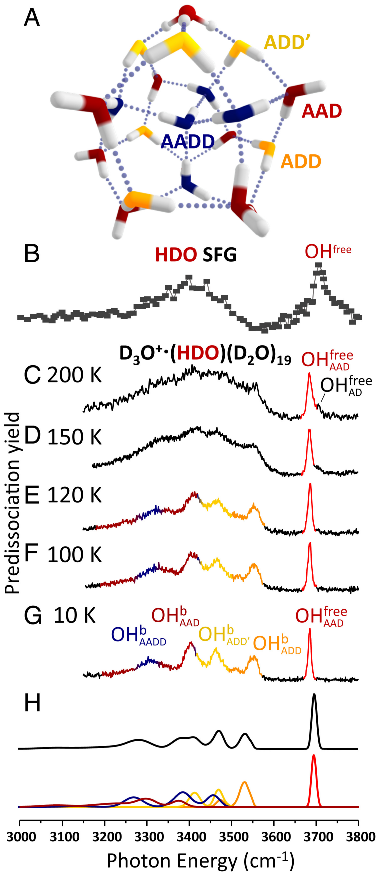

Figure 4.1: Comparison of the isotope-diluted SFG spectrum of the air-water interface with vibrational predissociation spectra of $D_3O^+ \cdot (HOD)(D_2O)_{19}$ at temperatures in the range 10 to 200 K. (A) Representative low-energy structure of the $H_3O^+ \cdot (H_2O)_{20}$ cluster. The stick spectra of the clusters with the OH group in each of the possible sites of the cluster are included in Figure 4.6. (B) SFG spectrum of HDO at the air-water interface. Reprinted with permission from ref. [74]. Copyright 2009 American Chemical Society. (C-G) Vibrational spectra of $D_3O^+ \cdot (HOD)(D_2O)_{19}$ from 200 to 10 K. OH^b and OH^{free} represent hydrogen-bonded OH and free OH. The A/D notation labels the number of hydrogen bond acceptors and donors on one water molecule. (H) displays the calculated spectrum based on 400 isotopomers of the 10 lowest energy structural isomers of the $D_3O^+ \cdot (HOD)(D_2O)_{19}$ cluster. The contribution from each type of water molecule (or site) to specific regions of the spectrum is colored to match the scheme in (A).

spectra in the OH stretching region[85]. The PDOH class occurs with many spectroscopically distinct isotopomers at low temperature according to the location of the unique OH group in the PD structure. This spectral variation occurs because the water molecule with the OH group is differentiated according to the number of H-bond donors (D) and acceptors (A) at play in each site, as well as the H-bonding topology of the more distant molecules in the network. We note that, because both intermolecular and intramolecular coupling are suppressed in the OH stretching spectra of the PDOH isotopomers, the resulting bands are dramatically simplified compared to those displayed by the homogeneous $\mathrm{H_3O^+ \cdot (H_2O)_{20}}$ isotopologue (SI Appendix, Figure S3)[85]. There are five clearly distinct OH bands in the PDOH spectrum that are color-coded in Figure 4.1G (full spectrum in SI Appendix, Figure S4) according to the specific sites that are calculated to yield fundamentals in the observed locations (Figure 4.6).

At low temperature, the spectrum of the mass-selected ion packet consists of a heterogeneous combination of the spectra of individual isotopomers, each of which can be isolated using isotopomer-selective vibrational spectroscopic methods as discussed at length in previous studies[86–89]. Isotopomer selection is achieved by sequentially removing each isotopomer from the ion packet through infrared (IR) photodissociation at each of the five band positions with an initial IR laser with pulse width 8 ns (hereafter denoted the "bleach" laser). Features in the spectrum that are modulated by the bleach are revealed by interrogating the same ion packet with a second IR laser pulse (8 ns pulse width, hereafter denoted the "probe" laser) that follows the bleach pulse after a delay time, Δt. Site-specific spectra for the five sites were reported previously and are reproduced in SI Appendix, Figure S3. The cold (T = 10 K) ensemble is static, such that photodestruction of an isotopomer permanently removes this species even when the ion packet is stored for long holding times (up to 1 s in the present study) in an ion trap. In this report, we explore the situation in which, as the temperature is elevated, the OH group is observed to spontaneously migrate from one site to another.

The strategy of our experimental approach was introduced in an earlier demonstration study of the $\mathrm{I^- \cdot (HDO) \cdot (D_2O)}$ cluster[88, 90, 91], where the OH oscillator was found to migrate between all four positions when warmed to 150 K. That system is sufficiently small that it could be accurately treated with high-level theory[91]. In this study, we explore the scenario presented by a larger water network in which the dynamics reflect different possible pathways for collective motions over a complex free energy landscape closer to that of condensed phase water. This scenario presents the possibility for sequential onsets of large-amplitude motions. Application to the present system involving five spectroscopically distinct sites is illustrated schematically in Figure 4.2. Each circle represents the population in one of the sites with the appropriate color as defined in Figure 4.1 A and G. The low-temperature case, which we exploited earlier to obtain the spectral signatures of OH in each site, is diagrammed in the top panel. Removal of population in the red sites by photodissociation leaves a static ensemble of the remaining ions. When the second laser probes the populations of the various other isomers at time Δt later, the four other features appear unaffected by the selective population removal by the first laser. As the temperature is increased, however, the OH group can migrate between sites. In the simplest case where only two sites interconvert (red and brown in Figure 4.2B), and the bleach laser's pulse width is short compared to the site-to-site exchange rate, the red population can be initially completely removed. This population partially recovers over time while the population in the brown state is reduced to achieve the ratio of populations in the two states dictated by the equilibrium constant. When steady state is restored at sufficiently long delay times, Δt, the populations of both red and brown sites will be reduced by half (assuming Keq = 1), while those in the other three sites are unaffected. This site-specific population redistribution scenario is depicted by partial refilling of the bleached circle after a delay time Δt in Figure 4.2B. The effect is observable in an experiment that monitors the modulations in the probe laser IR band intensities (and hence site populations) by the action of the bleach, which would yield diminution of the red and brown bands in the OH stretching region. The case where all sites interconvert at high temperature is diagrammed in Figure 4.2C. The initially depleted red site is repopulated by site exchange with all other four sites, yielding strong initial depletion of the red band followed by nearly complete recovery. All other bands are reduced to a lesser extent over time. In this case, the IR spectrum for the ensemble would appear the same as that before the depletion laser, but with all bands attenuated by the fraction of total red site population removed at t = 0.

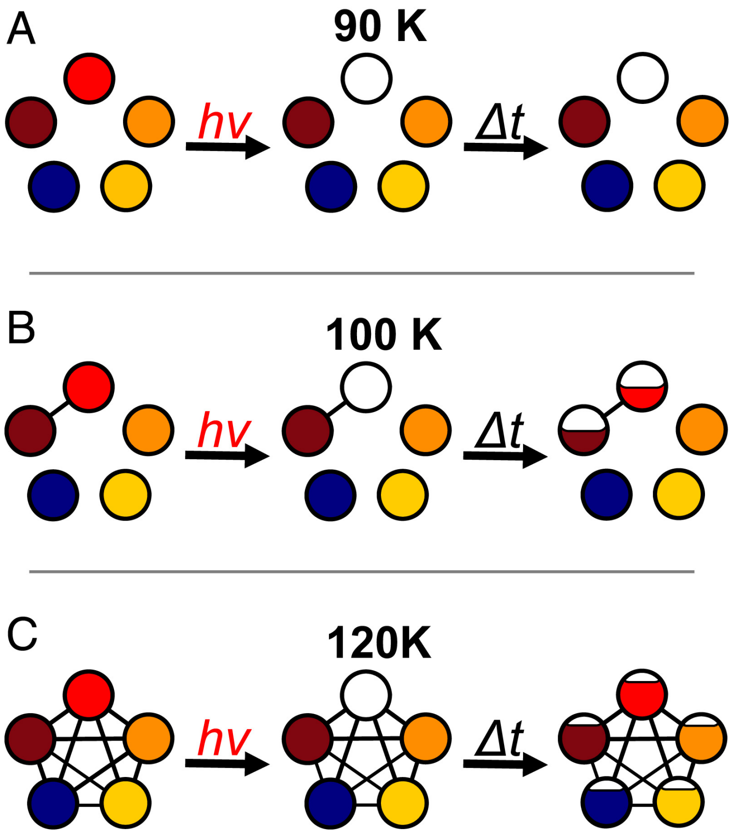

Figure 4.2: Scheme describing the onset of spectral diffusion by site exchange in a temperature-controlled cluster using selective photodissociation. The populations in the five spectroscopically distinct sites, color-coded to match those identified in Figure 4.1 (A) and (G), are indicated by the fractional filling of the circles. The panels correspond to three temperature regimes: (A) a low-temperature, static ensemble in which the red isotopomer is removed at $t = 0$, and subsequent interrogation of the ensemble after a delay time Δt reveals persistent removal of the red species from the ion packed; (B) an intermediate temperature where only two sites, red and brown, undergo interconversion on the timescale of the experiment. In this case, initial depletion of the red species, and hence its signature vibrational band, partially recovers after time Δt while the population of the brown isotopomer decreases to restore equilibrium with red; and (C) a sufficiently high temperature that all sites interconvert after initial depletion of red such that, after delay Δt, the red population is largely restored while those in the other four sites exhibit minor depletions upon returning to steady state.

The temperature-dependent measurements are carried out using a two-color, IR–IR photodissociation scheme. The experimental layout (SI Appendix, Figure S5) and details of the experimental approach are included in SI Appendix. Because the PD cluster is relatively large, the unimolecular rates for laser-induced evaporation are on the order of several milliseconds. These rates dictate the time delay between bleach and probe such that the clusters excited by the bleach laser are efficiently removed from the ion packet before it is explored by the probe. In that case, when the scanning bleach laser excites any transition that modulates the population of the site interrogated by the probe, that change is registered as a depletion (or dip) in the probe signal. We note that because the evaporation rates and spectral dynamics are so slow, excitation by the bleach laser is carried out while the ions are held in the temperature-controlled, three-dimensional radiofrequency ion trap, which enables trapping for long periods without loss.

To apply the temperature-dependent IR-IR photobleaching method to the PDOH clusters, it is important to first establish the temperature dependence of the linear IR spectrum, which is displayed in Figure 4.1. At 10 K, the spectrum consists of a well-resolved grouping of five bands. These have been traced to the various classes of H-bonding arrangements color-coded with structural assignments in Figure 4.1[87]. Interestingly, this five-band pattern persists up to 120 K before it recedes into a continuum envelope by 200 K, a temperature at which the clusters are unstable with respect to evaporation on the millisecond timescale of the mass spectrometer. For reference, the evaporation time (1/kevap) is measured to be 17 ms at 200 K as described in detail in SI Appendix, Figure S6. We note that the observed evolution of the spectra with temperature is consistent with nano-calorimetric measurements reported earlier[92] on $H_3O^+ \cdot (H_2O)_{20}$. In that case, an inflection in the caloric curve near 135 K was interpreted to signal the cluster analog of a melting transition, which occurs below the onset of evaporation at around 150 K[92–96]. We note also that recent molecular dynamics simulations of $H_3O^+ \cdot (H_2O)_{20}$ by Korchagina et al.[**korchagina**] indicate that the melting transition occurs over the 130 to 149 K range and that, although the PD structure dominates up to the melting region, cage structures containing four-membered rings begin to appear at 130 K. This is consistent with our temperature-dependent spectra, which display significant broadening of the bands as they are overcome by a diffuse background absorption between 120 and 150 K (Figure 4.1 D and E). Additionally, a shoulder appears about 18 cm^{-1} above the feature at 150 K, which signals the presence of AD water molecules and the disruption of the PD cage motif[97]. Meanwhile, the persistence of the telltale bands presented by the PD structure at 120 K establishes the integrity of this arrangement even when the clusters have substantial internal energy. For example, an estimate of the heat capacity at 120 K at the harmonic level (SI Appendix, Figure S10) indicates that the average internal energy is 2,400 cm^{-1}, which corresponds to about two-thirds of the energy required to dissociate a water molecule from the cluster (3,742 cm^{-1})[98, 99]. We note that there is a rather broad expected distribution of energies (ΔE   1,200 cm^{-1}) in an ensemble of ions held at constant T = 120 K. It is likely that this temperature is maintained by collisions with the residual He buffer gas in the trap[100, 101], which we estimate to be on the order of 10-4 torr at 120 K.

The Top panel in Figure 4.3 presents the time dependence of the two color, IR–IR spectra of the PDOH cluster at 120 K. The upper trace (Figure 4.3A) displays the changes in the site population, obtained by monitoring the probe laser fragment 40 μs after the bleach laser removes populations that have resonances at various energies along the course of the scan. The only dip feature occurs when the bleach laser excites the red ($\mathrm{OH_{AAD}}^{\mathrm{free}}$) transition, which is the behavior expected for a static, heterogeneous ensemble. Under exactly the same conditions of excitation, however, the response of the probe laser fragment yield is dramatically different after a bleach to probe delay of 50 ms, with the result displayed in Figure 4.3B. Indeed, depletion of red population is now obtained upon excitation of all five OH sites, with the result that the dip trace appears essentially the same as the linear spectrum of the entire ion isotopologue (purple lines through the points from the IR–IR scan in Figure 4.3B, reproduced from Figure 4.1E). This behavior is conclusive evidence that the spectrum associated with a single site at t = 0 evolves over time to encompass the contributions of all sites, which in turn establishes that the OH group migrates among all five locations. It is important to emphasize that this occurs while the overall spectrum retains the telltale bands of the PD cage. This implies that the migration is a rare event in the sense that the OH isotopic label almost always occupies a well-defined position in the cage. This general behavior was reported earlier in our initial study of temperature-dependent hole burning spectra of the much simpler $I^- \cdot (H_2O)_2$ system[90].

The two Lower panels in Figure 4.3 C and D present the time evolution of the depleted populations at two sites, one corresponding to the free OH (labeled $OH_{AAD}{}^{free}$), probed at 3,686 cm^{-1}, red, Figure 4.3D) and the other associated with OH occupation at the bound AAD site (labeled $OH_{AAD}{}^{b}$, and probed at 3,407 cm^{-1}, blue, Figure 4.3C). The different responses of these traces conform to the scenario outlined in Figure 4.2. Specifically, the large depletion initially present in the population of the red $OH_{AAD}{}^{free}$ site (Figure 4.3D) is gradually restored with a characteristic time constant of 19 ms, whereas a much smaller depletion in the population of site $OH_{AAD}{}^{b}$ occurs over similar time range (Figure 4.3C) as these OH groups migrate to the free OH site. Note that, although we have focused on only two positions in this discussion, at T = 120 K all sites are interchanging with the red site, as evidenced by the extensive dip pattern in Figure 4.3B. As such, the final fractional depletion in $OH_{AAD}{}^{free}$ (5%) is much smaller than the initial depletion (15%) since the other four sites contribute to compensate for the loss due to the bleach of the initial free OH site population.

The spectral evolution at 120 K is well described in the scheme where slow migration of the OH groups reequilibrates the populations in the ion packet on the 50-ms timescale. This raises the question, however, of whether the pathways that are available for this migration depend on the temperature of the ensemble. This might be anticipated, for example, if the free energy barriers are different for the rearrangements necessary for the OH to migrate between the various sites. We therefore determined the temperature dependence of the IR-IR dip spectra. A summary of the results is presented in Figure 4.4. At 90 K, the spectrum is dominated by a strong dip at the probe frequency, but by 100 K, there is a clear appearance of a weak, isolated second depletion feature near 3,350 cm^{-1}, about 300 cm^{-1} from the red band. Interestingly, the heat capacity curve observed with nanocalorimetry on the same cluster has a minor inflection point around 90 K[92]. This is consistent with the increase in phase space volume allowed by the onset of H-bond switching between the free OH and the bound OH on the same AAD water molecule that is implied here. Upon increasing the temperature to 110 K, it is clear that many more sites are exchanging with the probed red site, as the dip pattern (Figure 4.4E) includes many of the most red-shifted OH groups. This behavior is significant because it emphasizes that the frequency of an

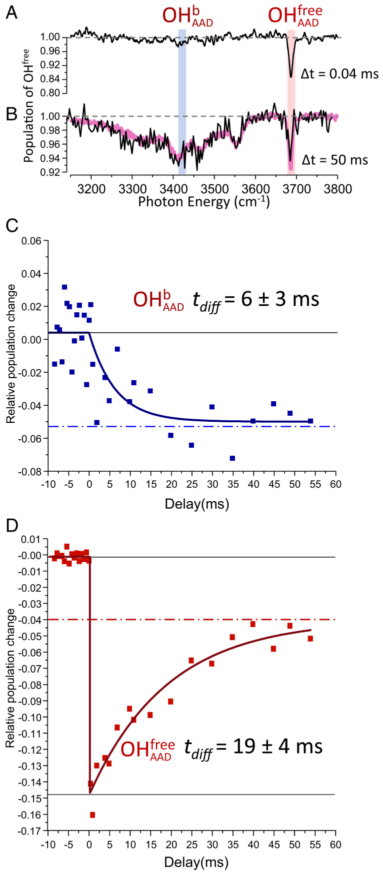

Figure 4.3: Time dependence of the $\mathrm{PD}_{\mathrm{OH}}$ IR spectrum following photodepletion of the isotopomer with the isotopically labeled OH group in the nonbonded (red) site $\mathrm{OH}_{\mathrm{AAD}}{}^{\mathrm{free}}$ at T = 120 K. Double sesonance spectra were obtained at bleach-probe delay times of (A) 0.04 ms and (B) 50 ms. The purple trace in (B) closely reproduces the single laser spectrum of the entire isotopologue (all sites occupied) from Figure 4.1E. The time evolutions of the $\mathrm{OH}_{\mathrm{AAD}}{}^{\mathrm{free}}$ population modulation by the bleach laser at two frequencies ($\mathrm{OH}_{\mathrm{AAD}}{}^{b}$ and $\mathrm{OH}_{\mathrm{AAD}}{}^{\mathrm{free}}$ in (A)) are presented in (C) and (D), respectively. The time constants t_{diff} were extracted from exponential fits to the observed data. Negative delay times in (C) and (D) correspond to experiments with the bleach laser off.

OH oscillator does not gradually broaden with time about the original location, but instead abruptly changes to another, distant frequency. The experimental results, discussed above, are consistent with a low barrier isomerization process initiated at T 100 K, and higher barrier processes being engaged above T = 120 K. We examine the barriers for rotation of a HOD molecule in the various sites of a $HDO \cdot (D_2O)_{20}$ cluster composed of a hydrogen-bonding network mimicking that of the $H_3O^+ \cdot (H_2O)_{20}$ cluster[102]. We focus on the neutral rather than the protonated cluster because of the availability of highly accurate force fields for the former. The lowest barrier pathway for rotation of a water molecule involves an AAD water donating an H bond to an adjacent AAD molecule. The lowest barrier associated with the AAD–AAD pair is consistent with its classification as a "weak" hydrogen bond on the surface of polyhedral water clusters[103]. As shown in Figure 4.9, this isomerization process is highly cooperative, involving the motion of several water molecules in the cluster. In addition, it proceeds through a stable intermediate with two four-membered and one three-membered ring, and a five-coordinated water molecule. The calculated vibrational frequencies of the HOD molecule in this site are in close agreement with those for the water molecule involved in the isomerization process that turns on at T = 100 K in the $D_3O^+ \cdot (HOD)(D_2O)_{19}$ cluster. Note that the bound OH stretching band associated with AAD water molecules that donate to another AAD molecule were observed to be 3,350 cm^{-1} in a previous study[86], which is indeed close to observed exchange feature that appears at 100 K (Figure 4.4D). The barriers for rotating the other water molecules are ¿1.3 kcal/mol (450 cm^{-1}) higher in energy than the one for the low-energy pathway described above, a fact that is consistent with the more extensive isomerization observed experimentally at temperatures above 120 K as well as the 1.8 kcal/mol (630 cm^{-1}) difference in activation energy obtained experimentally (SI Appendix, Figure S11).

Qualitatively, this large jump in frequencies at the onset of large-amplitude motion is reminiscent of models in which spectral diffusion reflects infrequent large-amplitude structural rearrangements rather than diffusive fluctuation about an initial configuration[75]. We also emphasize that the 120 K dip spectrum, displayed in Figure 4.4F, is effectively an inverted presentation of the linear spectrum of the entire ensemble at this temperature. The arrows in Figure 4.4 indicate the direction of population transfer responsible for the diminution of

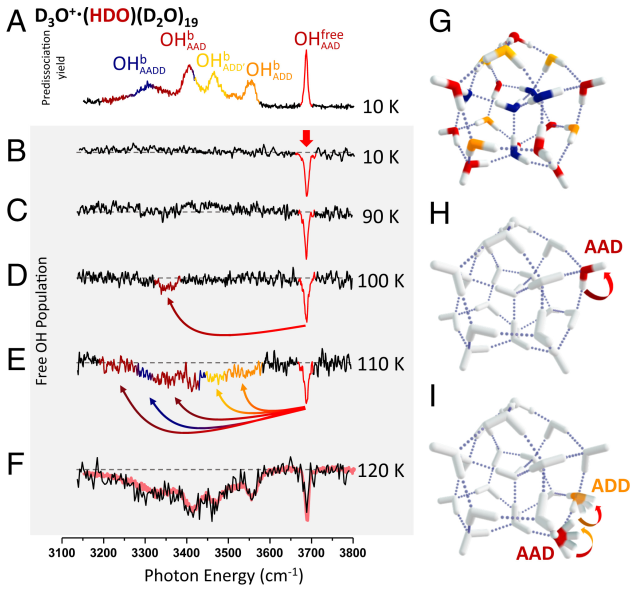

Figure 4.4: Temperature-dependent evolution of the photobleaching spectra corresponding to a bleach-probe delay of 50 ms and fixing the probe laser to monitor population of the isotopomer with the isotopically labeled OH group in the nonbonded (red) site ($\mathrm{OH_{AAD}}^{\mathrm{free}}$). (A) Vibrational spectrum of all isotopomers at 10 K and (B-F) hole burning spectra at 10 to 120 K. The red trace in (F) reproduces the single laser spectrum of the entire isotopologue (all sites occupied) from Figure 4.1E. The vertical red arrow in (B) indicates the probe laser frequency, whereas the curved arrows in (D) and (E) indicate that the apperance of additional dips arise from OH migration from the $\mathrm{OH_{AAD}}^{\mathrm{free}}$ site to various other sites when their populations are depleted by the bleach laser, (G) a representative low-energy PD structure, (H) a possible pathway for OH migration at 100 K, and (I) schematic illustration of more complex pathways that likely operate at higher temperatures where the ribbon arrows indicate the directions of the OH group rotations.

absorption at the probe (red) frequency. In this way, we reveal the hierarchy of site-to-site interconversions that are accessible with increasing temperature. A particularly interesting feature in this regard involves the band associated with water molecules that are directly attached to the hydronium ion core (labeled as ADD'), which begin to undergo exchange with the free OH site at 110 K. This is significant because transfer of these OH sites to those associated with more remote locations in the cage requires migration of the hydronium ion. As such, we conclude that 110 K also marks the onset of charge translocation across the cluster surface.

In summary, we have measured the time- and temperature-dependent frequency of a single OH oscillator embedded in the surface of the water cage structure adopted by 20 water molecules upon accommodation of the hydronium ion. Although the telltale vibrational signature of the cluster remains intact up to 120 K, the frequency of the OH group is observed to change over time, revealing migration between spectroscopically distinct sites. The timescale of this motion is on the order of tens of milliseconds, indicating that the rearrangements occur as rare events. The onset for dynamics is 100 K, at which point the frequency changes between two local features separated by about 300 cm^{-1}. All sites are interchanged on this timescale by 120 K, a significantly lower temperature than that at which the well-defined cluster structure is lost. This ability to monitor kinetic processes that sustain dynamic equilibrium in increasingly complex clusters brings us closer to applications where thermally activated chemical transformations can be unraveled in the context of both solvent and solute contributions at the molecular level.

4.4 Methods

The experimental methods are described in detail in SI Appendix, Section I. Briefly, the $D_3O^+ \cdot (HOD)_m(D_2O)_n$ clusters were generated by electrospraying acidic HDO/D_2O solution and passing the product ions through several stages of differential pumping and into a temperature-controlled Paul trap. The absorption spectra of the water clusters so generated were obtained using a photofragmentation mass spectrometer as described previously[88].

For isotopomer selective spectroscopy, the $D_3O^+ \cdot (HOD)(D_2O)_{19}$ clusters were first mass isolated with secular frequency excitation and then irradiated with a tunable IR laser (denoted the “bleach”) in the temperature-controlled Paul trap. After an adjustable waiting time, the ion packet is extracted from the Paul trap and passed into the Time-of-Flight photofragmentation mass spectrometer, where a second laser (denoted the “probe”) is intersected with the mass-selected ion packet to monitor the population in a specific isotopomer.

4.5 Discussion of Computational Methods and Results

The following sections were originally published in the Supporting Information of the main paper. They are included here due to their relevance to the rest of this work.

4.5.1 Computational Methods for the Structures and Vibrational Frequencies of $H^+ \cdot (D_2O)_{21}$

Detailed calculations on different H-bonding arrangements of $H_3O^+ \cdot (H_2O)_{20}$ with a pentagonal dodecahedral structure identify 10 structurally similar, low-energy isomers that are very close in energy (Figure 4.5). These structures minimize the number of dangling hydrogens on adjacent water monomers while having no dangling hydrogens adjacent to the H_3O^+ monomer. Seven of these isomers are known from earlier studies[73, 104]. Optimizations of the structures of the ten low-energy isomers were performed using the DF-MP2 method[48, 63, 105–108], where the ”DF” indicates the use of density fitting, in conjunction with the aug-cc-pVDZ basis set[49–52, 57, 58]. The DF-MP2/aug-cc-pVDZ optimized structures were used to calculate harmonic vibrational frequencies and intensities at the same level of theory[109]. The geometries were then reoptimized at the DF-MP2/aug-cc-pVTZ[48, 63, 105–108] level, with the resulting structures being used for subsequent single-point calculations at the DF-MP2/aug-cc-pVQZ[48, 63, 105–108] level of theory. All calculations were done using the Molpro 2018 package[67, 68]. Table 4.1 lists the relative energies of the ten isomers calculated at the DF-MP2/aug-cc-pVQZ level of theory.

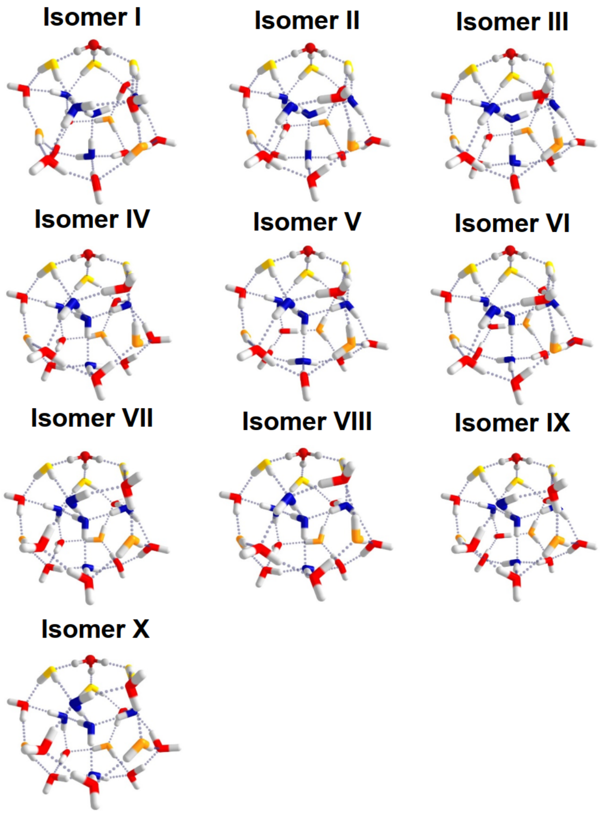

Figure 4.5: Structures of 10 low energy isomers of the $H_3O^+ \cdot (H_2O)_{20}$ species. These geometries are optimized at the DF-MP2/aug-cc-pVTZ level

Table 4.1: Relative energies of the lowest energy isomers of $H_3O^+ \cdot (H_2O)_{20}$. Energies are calculated at the DF-MP2/aug-cc-pVQZ level of theory, using geometries optimized at the DF-MP2/aug-cc-pVTZ level

Isomer	**Relative energy (kcal/mol)**
1	0.082
2	0.049
3	0.029
4	**0.000**
5	0.021
6	0.075
7	0.137
8	0.034
9	0.134
10	0.161

Vibrational frequencies were calculated for all 43 possible locations of H on each isomer, including on the hydronium monomer, for a total of 430 sets of frequencies. For the individual structural isomers, the spread in the relative zero-point energies (ZPEs) for the different isotopomers is only about 70 cm^{-1}, or 0.2 kcal/mol. This is close to the differences in the relative ZPEs of the ten $H_3O^+ \cdot (H_2O)_{20}$ isomers considered here.

In generating the calculated spectra reported in the main body of the text and in Figure 4.6, the frequencies were scaled by a factor of 0.96, which brings the calculated frequencies of the free OH transitions into close agreement with experiment. The OH stretch frequencies where the H atom is located on the hydronium monomer are 400 cm^{-1} lower in energy than the lowest frequency HOD OH stretch vibrations, and thus are not included in the calculated spectra used for comparison with experiment. The spectra from the remaining 400 isotopomers are given equal weight. Given their closeness in energy this should be a reasonable assumption for clusters at temperatures near or above 100 K.

4.5.2 Computational Results for $(H_2O)_{21}$

Figure 4.7 shows the 3D structure and the 2D Schlegel diagram of the lowest energy isomer of $(H_2O)_{21}$ with a PD cage and internal H_2O molecule identified to date[110]. The Schlegel diagram indicates the numbering of the water molecules used in this work.

Figure 4.8 displays the lowest energy pathways for rotation of each of the AAD molecules of $(H_2O)_{21}$. These results were obtained using the MB-pol potential[111] and were provided by D. Wales. They were confirmed by our own calculations carried out using the OPTIM code[112]. Note that each of these pathways involves two or three transition state structures, and, hence, one or two intermediate structures. All pathways include at least one 4-membered ring in the intermediate, except in the case of water 15 where the 4-membered ring appears in a TS. Additionally, at least one intermediate in each pathway, except in the case of water 4, includes a 5-coordinated water in the local minimum.

Figure 4.9 depicts using Schlegel diagrams the lowest energy rotational pathway (involving water 3) of $(H_2O)_{21}$. Table 4.2 reports the energies of the stationary points on the pathways for rotating each of the eight AAD water molecules of $(H_2O)_{21}$. Results are reported for the TTM-2.1-F[113] and MB-pol force fields, and in a subset of cases, also at the MP2/aug-cc-pVDZ level of theory. Vibrational zero-point energy (ZPE) corrections of the $(HOD)(D_2O)_{20}$ isoptopomers, calculated in the harmonic approximation are also indicated.

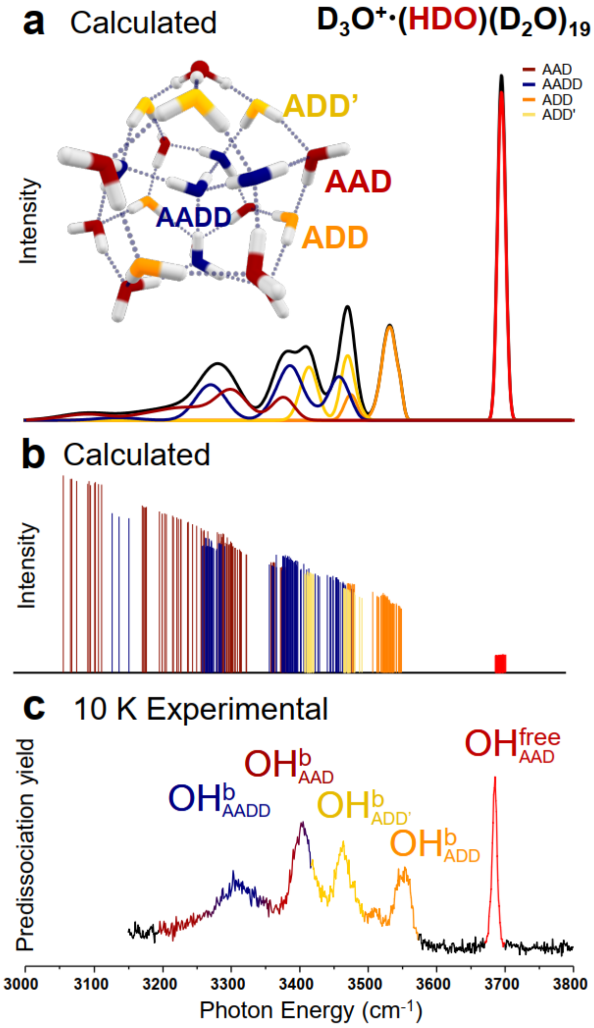

Figure 4.6: Comparison between calculated and experimental vibrational spectra of isotopomers of the $D_3O^+ \cdot (HDO)(D_2O)_{19}$ isotopologue. (a) Calculated spectra including summed contributions (black trace) from 400 isotopomers of the 10 low energy structural isomers shown in Figure 4.5 where scaled (0.96 scaling factor) harmonic frequencies are convolved with experimentally determined linewidths. Contributions from the various types of water molecules are displayed in color coded traces that correspond to the scheme depicted in the representative structure. (b) Calculated stick spectra. (c) Experimental spectrum at 10 K including contributions of all isotopomers present.

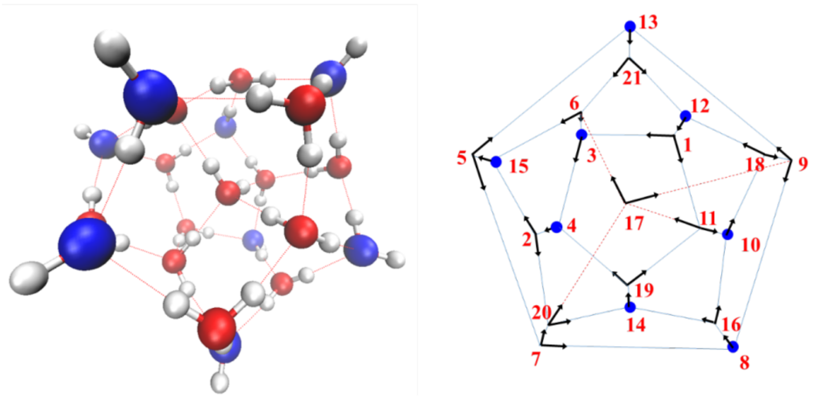

Figure 4.7: 3D structure and the 2D Schlegel diagram of the lowest energy isomer of $(H_2O)_{21}$. On the Schlegel diagram (right panel, a 2D projection of the 3D structure), each red number labels a water molecule's oxygen atom and black arrows point along the OH bond. Dotted red lines and thin blue lines are hydrogen bonds. Blue balls in the 3D structure (left panel) and blue dots in the Schlegel diagram (right panel) denote water molecules with a free OH group.

Table 4.2: Energies (kcal/mol) of transition states and intermediates for rotating the water molecules of $(H_2O)_{21}$ with a free OH group. Energies are referenced relative to the global minimum.

Pathway	**Method**	**TS1**	**Int. 1**	**TS 2**	**Int. 2**	**TS 3**
Water 3	TTM	4.73	1.50	2.70	-	-
	TTM + ZPE	3.61	0.78	2.08	-	-
	MBPol	3.90	1.54	2.94	-	-
	MBPol + ZPE	3.56	1.56	2.71	-	-
	MP2/AVDZ	-	2.20	-	-	-
Water 4	TTM	4.39	0.65	2.46	1.84	5.50
	TTM + ZPE	3.30	0.51	2.07	1.44	5.33

Pathway	**Method**	**TS1**	**Int. 1**	**TS 2**	**Int. 2**	**TS 3**
	MBPol	3.73	0.69	2.96	1.98	5.04
	MBPol + ZPE	3.35	0.70	2.78	2.11	4.69
	MP2/AVDZ	-	0.80	-	2.19	-
Water 8	TTM	6.06	2.92	4.00	-	-
	TTM + ZPE	4.78	2.85	3.37	-	-
	MBPol	4.77	2.85	3.37	-	-
	MBPol + ZPE	4.47	3.41	4.38	-	-
	MP2/AVDZ	-	3.57	-	-	-
Water 10	TTM	6.63	5.19	6.84	-	-
	TTM + ZPE	5.39	4.75	6.07	-	-
	MBPol	6.06	5.95	6.32	-	-
	MBPol + ZPE	5.75	5.74	5.90	-	-
	MP2/AVDZ	-	5.47	-	-	-
Water 12	TTM	5.31	2.45	5.00	4.75	5.46
	TTM + ZPE	4.32	2.03	4.99	4.81	5.35
	MBPol	6.34	2.56	4.14	4.03	4.46
	MBPol + ZPE	5.91	2.71	3.95	3.89	4.09
	MP2/AVDZ	-	3.29	-	4.77	-
Water 13	TTM	7.00	2.20	7.00	-	-
	TTM + ZPE	5.76	1.52	6.36	-	-
	MBPol	5.66	2.46	6.34	-	-
	MBPol + ZPE	5.12	2.44	5.98	-	-
	MP2/AVDZ	-	2.48	-	-	-
Water 14	TTM	4.90	3.88	4.91	-	-
	TTM + ZPE	3.69	3.20	4.57	-	-
	MBPol	6.04	4.21	4.36	-	-
	MBPol + ZPE	5.73	4.04	4.00	-	-
	MP2/AVDZ	-	4.93	-	-	-
Water 15	TTM	7.06	3.84	4.38	-	-

Pathway	**Method**	**TS1**	**Int. 1**	**TS 2**	**Int. 2**	**TS 3**
	TTM + ZPE	5.68	3.39	4.37	-	-
	MBPol	6.38	4.22	4.94	-	-
	MBPol + ZPE	5.95	4.15	4.61	-	-
	MP2/AVDZ	-	4.64	-	-	-

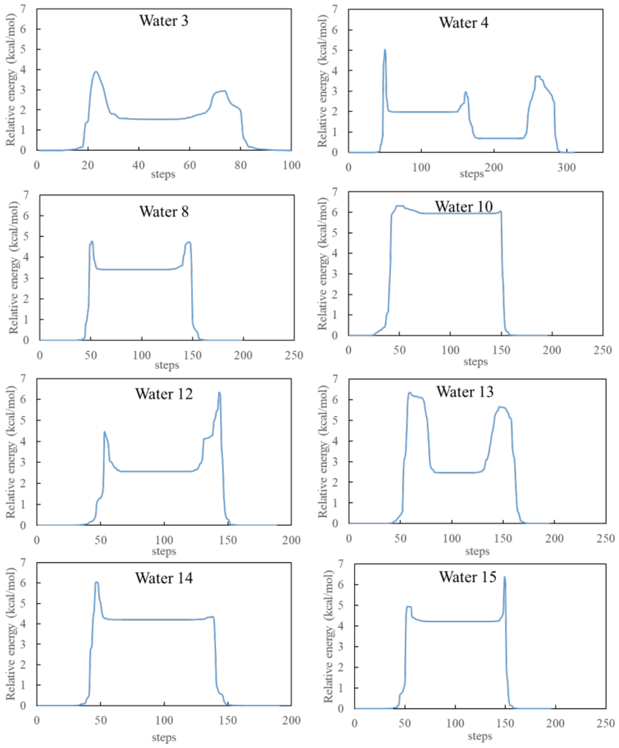

Figure 4.8: The lowest energy pathways for rotation of each of the AAD molecules of $(H_2O)_{21}$. The relative energies are calculated with MBPol.

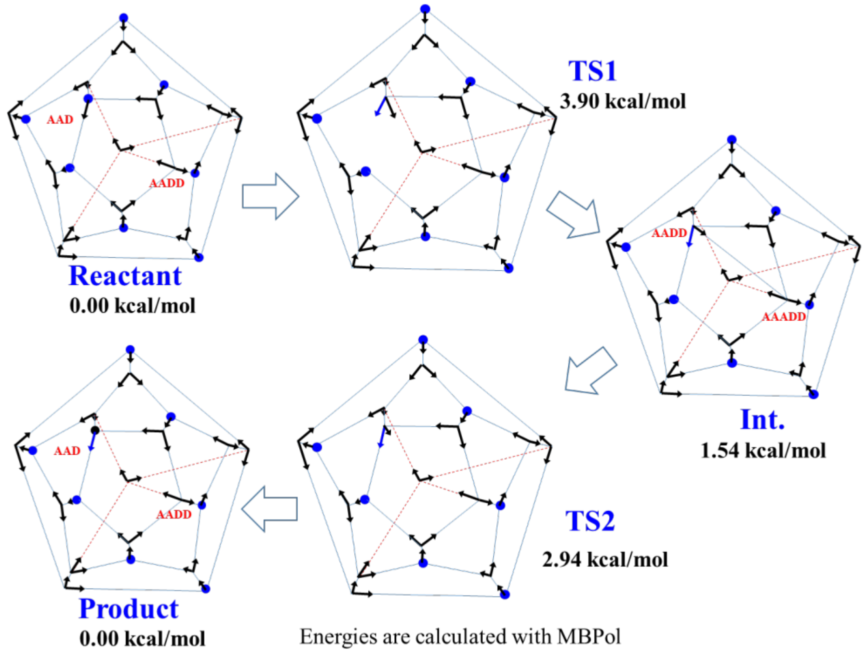

Figure 4.9: Schlegel diagrams for the lowest energy rotational pathway of water 3 (see Figure 4.7) of $(H_2O)_{21}$. The blue donts denote water molecules with a free OH group, the arrows label OH groups and the thinner lines represent hydrogen bonds. The water molecule labeled AAD in the reactant panel is the water molecule of interest that rearranges to exchange its free and bound OH groups. One of the original AAD water molecule's OH (black arrow) forms an additional hydrogen bond to the original AADD water molecule to form a four-membered ring involving a five coordinated AAADD water molecule

5.0 Summary and Future Work

This work used state-of-the-art theoretical methods to understand the vibrational spectra and isomerization dynamics of select water-ion clusters. The first paper illustrated the use of a one-dimensional adiabatic model for calculating vibrational progressions in water-anion clusters of the form $X^- \cdot (H_2O)$. Several different variants of the model were explored to see the impact of different techniques. Of note, it was found that using a double-well rock potential for the $N = 1$ rock potentials produced spectra which qualitatively matched key aspects of the experimental spectra, such as the length of the progressions. However, the spacing between peaks in the progression was overestimated by 15 cm^{-1} or more, showing there was room for improvement to achieve quantitative accuracy.

To improve the accuracy of the adiabatic model, the model was extended to include both intermolecular rock angles. Explicitly accounting for this additional degree of freedom produced near-quantitative agreement with experiment. This demonstrates the viability of using multi-dimension adiabatic models for investigating coupling between low and high frequency vibrational modes.

One clear application for these low dimensional adiabatic models is in modeling the spectra of larger water-anion clusters, particularly those with more than one water monomer. One cluster which can be logically used for extensions of this model is ${NO_3}^- \cdot (H_2O)_2$, which has a minimum energy structure similar to ${NO_3}^- \cdot (H_2O)$[114]. Although both water monomers are chemically identical, the presence of two water molecules will affect the charge distribution on the ${NO_3}^-$ anion, which will impact the shape of the adiabatic potentials. Additionally, the water monomers may be close enough to cause coupling between the rock mode on one monomer and the OH stretch mode on the other. Finally, both water rock modes will be coupled to the anion rock mode. There are four possible models that should be investigated: a 1D model along a single water rock, a 2D model of the two water rock modes where the anion rock is relaxed, a 2D model of one water rock and the anion rock where the other water rock is relaxed, and a 3D model along all three coordinates. Comparing results from all four models will provide insight into the coupling of low and high frequency modes in clusters with more than two monomers. This will provide insight into the types of intermolecular coordinates which are necessary to explicitly model as even larger systems are investigated.

Coupling between low and high frequency modes is not unique to small molecule clusters. Experimental studies have found "Franck-Condon" like vibrational progressions in small peptides[41, 115, 116]. Computational study of these progressions using a simple model has been used to verify the conformation of peptide structures[41]. These progressions result from a coupling between high frequency NH stretches and low frequency torsional modes. Progressions can also occur in microsolvated peptides from the interaction between the peptide and solvent monomer[116]. These types of vibrational progressions likely appear in many proteins, and even a sequence with as few as four amino acids can show two separate progressions[41]. Because of this, high accuracy models may be required to accurately distinguish different progressions. Therefore, low dimensional adiabatic models like the ones presented here may be a valuable tool in reproducing experimental vibrational spectra in cases where a simpler model is not sufficient.

As larger systems are studied or higher dimensional models are used, the computational cost of an adiabatic model becomes a greater concern. The majority of the computational work in these models is the optimizations and harmonic frequency calculations required to generate the adiabatic potentials. Therefore, the greatest computational gains can be achieved by either reducing the number of points along the potential that need to be calculated explicitly or by reducing the computational load for each individual point. The former could be accomplished by calculating a lower density of points in higher energy regions of the potential energy surface, as these regions have little impact on the first few energy levels. Reducing the computational cost of each point is trickier, as certain approximations will be more valid for certain systems. However, one possible approach would be to calculate the harmonic frequencies with a local mode approximation and calculate only the modes whose frequencies strongly depend on the adiabatic coordinates. For example, in $HCO_2^- \cdot (H_2O)$ and $NO_3^- \cdot (H_2O)$, the frequencies of the intramolecular anion vibrations change very little at different points of θ and ϕ, and thus have very little impact on the shape of the adiabatic potentials. To test the impact of these cost saving strategies on the accuracy of the final results, the already established results for $HCO_2^- \cdot (H_2O)$ and $NO_3^- \cdot (H_2O)$ can be used for comparison. While improving computational costs does not grant any new physical insight, it will likely be necessary for tackling new problems as the use of adiabatic vibrational models continues.

In the final study, computational techniques were used to aid in the study of rearrangement pathways in $D^+ \cdot (HOD)(D_2O)_{20}$. Electronic structure calculations were used to determine the most favorable class of structural isomers, and vibrational calculations were used on these structures to verify peak assignment from the experimental spectrum. More notably, pathway searching techniques were used to determine the pathway for the experimentally observed rotation of the HOD monomer. The existence of intermediate states with a four-membered ring demonstrates why rotation of the HOD monomer is more favorable than other rearrangement pathways. One limitation of this study was that the pathways were found on the neutral W_{21} cluster instead of the protonated cluster. While this is not expected to have much impact on the pathway itself, it may have some effect on the relative energies of the transition and intermediate states.

Although the rotation of an ADD water appears to be the most favorable rearrangement pathway in $H^+ \cdot (H_2O)_{21}$ clusters, it is far from the only type of rearrangement of interest to researchers. One interesting area of further study is the rearrangement of $H^+ \cdot (H_2O)_{21}$ from one structural isomer to another. In chapter 4.5, the 10 lowest energy isomers of $H^+ \cdot (H_2O)_{21}$ are shown. Other structural isomers contain either more adjacent AAD waters, or AAD waters bound to H_3O^+, both of which increase the energy of the cluster by at least 2 kcal/mol. This poses the question of which pathway is more favorable for the conversion of one low energy isomer to another: a pathway going through one of these higher energy isomers, or one which goes through a non-dodecahedral intermediate structure. Knowing these pathway will increase the understanding of the dynamics in these clusters, which will improve the interpretation of experimental data.

One of the major motivations in studying water-ion clusters is that understanding of molecular-level interactions will provide insight into solvation interactions in the bulk water system. This will accomplished by developing experimental and theoretical methods to precisely and accurately study small clusters. As new experiments are developed and available computing power increases, larger and larger clusters can be studied, with properties that approach those of the bulk solution. This is a highly active area of research, and experimental advancements are happening at a rapid pace. Therefore, it is vital that computational understanding is able to keep up with experimental developments, either by using established methods to study new experimental results, or by developing new computational approaches with more well-understood systems. The three papers presented in this thesis use both of these approaches to add a piece to this exciting and ongoing area of study.

6.0 Bibliography

(1) Bohr, N. *Nature* **1925**, *116*, 845–852.

(2) Werner, H. *Zeitschrift für Physik* **1925**, *33*, 879–893.

(3) Wilson, E. B.; Decius, J. C.; Cross, P. C., *Molecular vibrations: the theory of infrared and Raman vibrational spectra*; Courier Corporation: 1980.

(4) Noid, D.; Koszykowski, M.; Marcus, R. *Journal of Chemical Education* **1980**, *57*, 624.

(5) Nielsen, H. H. *Physical Review* **1941**, *60*, 794.

(6) Wilson, E. B. *J. Chem. Phys.* **1939**, *7*, 1047–1052.

(7) Podolsky, B. *Phys. Rev.* **1928**, *32*, 812.

(8) Eckart, C. *Physical Review* **1935**, *47*, 552.

(9) Louck, J. D.; Galbraith, H. W. *Reviews of Modern Physics* **1976**, *48*, 69.

(10) Light, J. C.; Carrington, T. *Advances in Chemical Physics* **2007**, *114*, 263–310.

(11) Stare, J.; Balint-Kurti, G. G. *J. Phys. Chem. A* **2003**, *107*, 7204–7214.

(12) Balint-Kurti, G. G.; Dixon, R. N.; Marston, C. C. *Int. Rev. Phys. Chem.* **1992**, *11*, 317–344.

(13) Heine, N.; Kratz, E. G.; Bergmann, R.; Schofield, D. P.; Asmis, K. R.; Jordan, K. D.; McCoy, A. B. *J. Phys. Chem. A* **2014**, *118*, 8188–8197.

(14) Robertson, W. H.; Price, E. A.; Weber, J. M.; Shin, J.-W.; Weddle, G. H.; Johnson, M. A. *J. Phys. Chem. A* **2003**, *107*, 6527–6532.

(15) Ayotte, P.; Weddle, G. H.; Kim, J.; Kelley, J.; Johnson, M. A. *The Journal of Physical Chemistry A* **1999**, *103*, 443–447.

(16) Johnson, M. S.; Kuwata, K. T.; Wong, C.-K.; Okumura, M. *Chemical physics letters* **1996**, *260*, 551–557.

(17) Gerardi, H. K.; DeBlase, A. F.; Su, X.; Jordan, K. D.; McCoy, A. B.; Johnson, M. A. *J. Phys. Chem. Lett.* **2011**, *2*, 2437–2441.

(18) Craig, S. M.; Menges, F. S.; Duong, C. H.; Denton, J. K.; Madison, L. R.; McCoy, A. B.; Johnson, M. A. *Proc. Natl. Acad. Sci. U. S. A.* **2017**, *114*, E4706–E4713.

(19) Myshakin, E. M.; Jordan, K. D.; Sibert, E. L.; Johnson, M. A. *J. Chem. Phys.* **2003**, *119*, 10138–10145.

(20) Hamm, P.; Stock, G. *J. Chem. Phys.* **2015**, *143*, 134308.

(21) Hagena, O.; Obert, W. *The Journal of Chemical Physics* **1972**, *56*, 1793–1802.

(22) Narcisi, R. S.; Roth, W. In *Advances in Electronics and Electron Physics*; Elsevier: 1970; Vol. 29, pp 79–113.

(23) Searcy, J.-Q.; Fenn, J. *The Journal of Chemical Physics* **1974**, *61*, 5282–5288.

(24) Zwier, T. S. *Science* **2004**, *304*, 1119–1120.

(25) Eigen, M. *Angewandte Chemie International Edition in English* **1964**, *3*, 1–19.

(26) Zundel, G.; Metzger, H. *Z. Phys. Chem* **1968**, *58*, 225–245.

(27) Duong, C. H.; Yang, N.; Kelleher, P. J.; Johnson, M. A.; DiRisio, R. J.; McCoy, A. B.; Yu, Q.; Bowman, J. M.; Henderson, B. V.; Jordan, K. D. *The Journal of Physical Chemistry A* **2018**, *122*, 9275–9284.

(28) Carpenter, W. B.; Yu, Q.; Hack, J. H.; Dereka, B.; Bowman, J. M.; Tokmakoff, A. *The Journal of Chemical Physics* **2020**, *153*, 124506.

(29) Shin, J.-W.; Hammer, N.; Diken, E.; Johnson, M.; Walters, R.; Jaeger, T.; Duncan, M.; Christie, R.; Jordan, K. D. *Science* **2004**, *304*, 1137–1140.

(30) Miyazaki, M.; Fujii, A.; Ebata, T.; Mikami, N. *Science* **2004**, *304*, 1134–1137.

(31) Daly Jr, C. A.; Streacker, L. M.; Sun, Y.; Pattenaude, S. R.; Hassanali, A. A.; Petersen, P. B.; Corcelli, S. A.; Ben-Amotz, D. *The Journal of Physical Chemistry Letters* **2017**, *8*, 5246–5252.

(32) Yu, Q.; Carpenter, W. B.; Lewis, N. H.; Tokmakoff, A.; Bowman, J. M. *The Journal of Physical Chemistry B* **2019**, *123*, 7214–7224.

(33) O'Brien, J. T.; Williams, E. R. *Journal of the American Chemical Society* **2012**, *134*, 10228–10236.

(34) Mizuse, K.; Mikami, N.; Fujii, A. *Angewandte Chemie International Edition* **2010**, *49*, 10119–10122.

(35) Zeng, H. J.; Yang, N.; Johnson, M. A. *Faraday Discussions* **2019**, *217*, 8–33.

(36) Guasco, T. L.; Johnson, M. A. In *Emerging Trends in Chemical Applications of Lasers*; ACS Publications: 2021, pp 277–306.

(37) Weber, J. M.; Kelley, J. A.; Robertson, W. H.; Johnson, M. A. *J. Chem. Phys.* **2001**, *114*, 2698–2706.

(38) Myshakin, E. M.; Jordan, K. D.; Robertson, W. H.; Weddle, G. H.; Johnson, M. A. *J. Chem. Phys.* **2003**, *118*, 4945–4953.

(39) Elliott, B. M.; Relph, R. A.; Roscioli, J. R.; Bopp, J. C.; Gardenier, G. H.; Guasco, T. L.; Johnson, M. A. *J. Chem. Phys.* **2008**, *129*, 094303.

(40) Kelly, J. T.; Mayer, M.; Kennedy, A. C.; Schemel, C.; Asmis, K. R. *J. Chem. Phys.* **2018**, *148*, 222840.

(41) Zabuga, A. V.; Kamrath, M. Z.; Rizzo, T. R. *J. Phys. Chem. A* **2015**, *119*, 10494–10501.

(42) Relph, R. A.; Elliott, B. M.; Weddle, G. H.; Johnson, M. A.; Ding, J.; Jordan, K. D. *J. Phys. Chem. A* **2009**, *113*, 975–981.

(43) Sokolov, N.; Savel'ev, V. *Chem. Phys.* **1977**, *22*, 383–399.

(44) Epa, V.; Thorson, W. *J. Chem. Phys.* **1990**, *92*, 473–488.

(45) McKenzie, R. H.; Bekker, C.; Athokpam, B.; Ramesh, S. G. *J. Chem. Phys.* **2014**, *140*, 174508.

(46) Stare, J. *J. Chem. Inf. Model.* **2007**, *47*, 840–850.

(47) Rush, D. J.; Wiberg, K. B. *J. Phys. Chem. A* **1997**, *101*, 3143–3151.

(48) Møller, C.; Plesset, M. S. *Phys. Rev.* **1934**, *46*, 618–622.

(49) Eichkorn, K.; Treutler, O.; Öhm, H.; Häser, M.; Ahlrichs, R. *Chem. Phys. Lett.* **1995**, *240*, 283–290.

(50) Eichkorn, K.; Weigend, F.; Treutler, O.; Ahlrichs, R. *Theor. Chem. Acc.* **1997**, *97*, 119–124.

(51) Eichkorn, K.; Treutler, O.; Oehm, H.; Häser, M.; Ahlrichs, R. *Chem. Phys. Lett.* **1995**, *240*, 283–290.

(52) Weigend, F. *Phys. Chem. Chem. Phys.* **2006**, *8*, 1057–1065.

(53) Weigend, F. *Phys. Chem. Chem. Phys.* **2002**, *4*, 4285–4291.

(54) Weigend, F.; Häser, M. *Theor. Chem. Acc.* **1997**, *97*, 331–340.

(55) Hättig, C.; Hellweg, A.; Köhn, A. *Phys. Chem. Chem. Phys.* **2006**, *8*, 1159–1169.

(56) Weigend, F.; Häser, M.; Patzelt, H.; Ahlrichs, R. *Chem. Phys. Lett.* **1998**, *294*, 143–152.

(57) Dunning, T. H. *J. Chem. Phys.* **1989**, *90*, 1007–1023.

(58) Kendall, R. A.; Dunning, T. H.; Harrison, R. J. *J. Chem. Phys.* **1992**, *96*, 6796–6806.

(59) Adler, T. B.; Knizia, G.; Werner, H.-J. A simple and efficient CCSD(T)-F12 approximation, 2007.

(60) Werner, H.-J.; Knizia, G.; Manby, F. R. *Mol. Phys.* **2011**, *109*, 407–417.

(61) Győrffy, W.; Knizia, G.; Werner, H.-J. *J. Chem. Phys.* **2017**, *147*, 214101.

(62) Győrffy, W.; Werner, H.-J. *J. Chem. Phys.* **2018**, *148*, 114104.

(63) Schutz, M.; Lindh, R.; Werner, H.-J. *Mol. Phys.* **1999**, *96*, 719–733.

(64) Peterson, K. A.; Adler, T. B.; Werner, H.-J. *J. Chem. Phys.* **2008**, *128*, 084102.

(65) Ahlrichs, R.; Bär, M.; Häser, M.; Horn, H.; Kölmel, C. *Chem. Phys. Lett.* **1989**, *162*, 165–169.

(66) TURBOMOLE V7.2 2017, a development of University of Karlsruhe and Forschungszentrum Karlsruhe GmbH, 1989-2007,TURBOMOLE GmbH, since 2007; available from
`http://www.turbomole.com`.

(67) Werner, H.-J.; Knowles, P. J.; Knizia, G.; Manby, F. R.; Schütz, M. *WIREs Comput. Mol. Sci.* **2012**, *2*, 242–253.

(68) Werner, H.-J. et al. MOLPRO, version 2019.1, a package of ab initio programs, 2019.

(69) Werner, H.-J.; Knowles, P. J.; Knizia, G.; Manby, F. R.; Schütz, M., et al. MOLPRO, version 2019.1, a package of ab initio programs, see, 2019.

(70) Brancato, G.; Rega, N.; Barone, V. *The Journal of chemical physics* **2008**, *128*, 04B607.

(71) Fattebert, J.-L.; Lau, E. Y.; Bennion, B. J.; Huang, P.; Lightstone, F. C. *Journal of Chemical Theory and Computation* **2015**, *11*, 5688–5695.

(72) Price, W. D.; Schnier, P. D.; Jockusch, R. A.; Strittmatter, E. F.; Williams, E. R. *Journal of the American Chemical Society* **1996**, *118*, 10640–10644.

(73) Xantheas, S. S. *The Canadian Journal of Chemical Engineering* **2012**, *90*, 843–851.

(74) Tian, C.-S.; Shen, Y. R. *Journal of the American Chemical Society* **2009**, *131*, 2790–2791.

(75) Laage, D.; Stirnemann, G.; Sterpone, F.; Hynes, J. T. *Accounts of chemical research* **2012**, *45*, 53–62.

(76) Ni, Y.; Gruenbaum, S. M.; Skinner, J. L. *Proceedings of the National Academy of Sciences* **2013**, *110*, 1992–1998.

(77) Ojha, D.; Kaliannan, N. K.; Kühne, T. D. *Communications Chemistry* **2019**, *2*, 1–7.

(78) Inoue, K.-i.; Nihonyanagi, S.; Singh, P. C.; Yamaguchi, S.; Tahara, T. *The Journal of Chemical Physics* **2015**, *142*, 212431.

(79) Cyran, J. D.; Backus, E. H.; Nagata, Y.; Bonn, M. *The Journal of Physical Chemistry B* **2018**, *122*, 3667–3679.

(80) Eaves, J.; Loparo, J.; Fecko, C. J.; Roberts, S.; Tokmakoff, A.; Geissler, P. *Proceedings of the National Academy of Sciences* **2005**, *102*, 13019–13022.

(81) Fecko, C.; Eaves, J.; Loparo, J.; Tokmakoff, A.; Geissler, P. *Science* **2003**, *301*, 1698–1702.

(82) Eigen, M. *Nobel Lecture* **1967**, *11*, 1963–1979.

(83) Kirov, M. *Journal of Structural Chemistry* **2002**, *43*, 790–797.

(84) Yu, Q.; Bowman, J. M. *The Journal of Physical Chemistry A* **2020**, *124*, 1167–1175.

(85) Fournier, J. A.; Johnson, C. J.; Wolke, C. T.; Weddle, G. H.; Wolk, A. B.; Johnson, M. A. *Science* **2014**, *344*, 1009–1012.

(86) Yang, N.; Duong, C. H.; Kelleher, P. J.; McCoy, A. B.; Johnson, M. A. *Science* **2019**, *364*, 275–278.

(87) Yang, N.; Duong, C. H.; Kelleher, P. J.; Johnson, M. A. *Nature Chemistry* **2020**, *12*, 159–164.

(88) Yang, N.; Duong, C. H.; Kelleher, P. J.; Johnson, M. A.; McCoy, A. B. *Chemical Physics Letters* **2017**, *690*, 159–171.

(89) Wolke, C. T.; Fournier, J. A.; Miliordos, E.; Kathmann, S. M.; Xantheas, S. S.; Johnson, M. A. *The Journal of Chemical Physics* **2016**, *144*, 074305.

(90) Yang, N.; Duong, C. H.; Kelleher, P. J.; Johnson, M. A. *The Journal of Physical Chemistry Letters* **2018**, *9*, 3744–3750.

(91) Bajaj, P.; Richardson, J. O.; Paesani, F. *Nature chemistry* **2019**, *11*, 367–374.

(92) Boulon, J.; Braud, I.; Zamith, S.; Labastie, P.; L'Hermite, J.-M. *The Journal of Chemical Physics* **2014**, *140*, 164305.

(93) Calvo, F.; Douady, J.; Spiegelman, F. *The Journal of chemical physics* **2010**, *132*, 024305.

(94) Dunbar, R. C. *Mass spectrometry reviews* **2004**, *23*, 127–158.

(95) Niedner-Schatteburg, G.; Bondybey, V. E. *Chemical Reviews* **2000**, *100*, 4059–4086.

(96) Schmidt, M.; von Issendorff, B. *The Journal of Chemical Physics* **2012**, *136*, 164307.

(97) Stachl, C. N.; Williams, E. R. *The Journal of Physical Chemistry Letters* **2020**, *11*, 6127–6132.

(98) Magnera, T. F.; David, D. E.; Michl, J. *Chemical Physics Letters* **1991**, *182*, 363–370.

(99) Shi, Z.; Ford, J.; Wei, S.; Castleman Jr, A. *The Journal of chemical physics* **1993**, *99*, 8009–8015.

(100) Vazquez, T.; Taylor, C.; Evans-Nguyen, T. *Analytical chemistry* **2018**, *90*, 10600–10606.

(101) Harrilal, C. P.; DeBlase, A. F.; Fischer, J. L.; Lawler, J. T.; McLuckey, S. A.; Zwier, T. S. *The Journal of Physical Chemistry A* **2018**, *122*, 2096–2107.

(102) Rakshit, A.; Bandyopadhyay, P.; Heindel, J. P.; Xantheas, S. S. *The Journal of chemical physics* **2019**, *151*, 214307.

(103) Kirov, M. V.; Fanourgakis, G. S.; Xantheas, S. S. *Chemical Physics Letters* **2008**, *461*, 180–188.

(104) Hodges, M. P.; Wales, D. J. *Chemical Physics Letters* **2000**, *324*, 279–288.

(105) El Azhary, A.; Rauhut, G.; Pulay, P.; Werner, H.-J. *The Journal of chemical physics* **1998**, *108*, 5185–5193.

(106) Werner, H.-J.; Manby, F. R.; Knowles, P. J. *The Journal of chemical physics* **2003**, *118*, 8149–8160.

(107) Polly, R.; Werner*, H.-J.; Manby, F. R.; Knowles, P. J. *Molecular Physics* **2004**, *102*, 2311–2321.

(108) Eckert, F.; Pulay, P.; Werner, H.-J. *Journal of computational chemistry* **1997**, *18*, 1473–1483.

(109) Hrenar, T.; Rauhut, G.; Werner, H.-J. *The Journal of Physical Chemistry A* **2006**, *110*, 2060–2064.

(110) Lagutschenkov, A.; Fanourgakis, G. S.; Niedner-Schatteburg, G.; Xantheas, S. S. *The Journal of chemical physics* **2005**, *122*, 194310.

(111) Babin, V.; Leforestier, C.; Paesani, F. *Journal of chemical theory and computation* **2013**, *9*, 5395–5403.

(112) Wales, D. *See http://www-wales. ch. cam. ac. uk/OPTIM* **1999**.

(113) Fanourgakis, G. S.; Xantheas, S. S. *The Journal of Physical Chemistry A* **2006**, *110*, 4100–4106.

(114) Li, H.; Kong, X.; Jiang, L.; Liu, Z.-F. *Physical Chemistry Chemical Physics* **2018**, *20*, 26918–26925.

(115) Stearns, J. A.; Seaiby, C.; Boyarkin, O. V.; Rizzo, T. R. *Physical Chemistry Chemical Physics* **2009**, *11*, 125–132.

(116) Fischer, K. C.; Voss, J. M.; Zhou, J.; Garand, E. *The Journal of Physical Chemistry A* **2018**, *122*, 8213–8221.